Observational issues in radiometric and interferometric detection and analysis of the Sunyaev-Zel'dovich effects

M. Birkinshaw and K. Lancaster

Department of Physics, University of Bristol, Tyndall Avenue, Bristol BS8 1TL, U.K.

1. – Single-dish and interferometric observations

Radiometric observations using single dishes and interferometers are responsible for most detections of the Sunyaev-Zel'dovich (SZ) effects. This article discusses the techniques used in measuring the thermal and kinematic SZ effects in this way, the pitfalls that may arise, the systematic errors in the data, and the resulting uncertainties in the interpretation of the results. Since these uncertainties limit the physics return from SZ effect research, some approaches that would improve this situation are described. Longer reviews of SZ effect research (Rephaeli 1995; Birkinshaw 1999; Carlstrom, Holder and Reese 2002) may be consulted for additional details.

1˙1. *Radiometric quantities.* – In discussing radiometric observations it is conventional to work with the flux density (S_ν, the energy received per unit time per unit frequency per unit area) as the measure of the brightness of an unresolved source. However, the SZ effects of clusters of galaxies are extended, and so a measure of surface brightness is more appropriate. Two such quantities are in general use. The flux density per unit solid angle, Σ_ν, is commonly adopted in describing interferometric observations, where the solid angle is usually the area of the synthesized beam. The brightness temperature, T_{RJ}, is more usual in single-dish work.

Flux density per unit solid angle and brightness temperature are related by

$$\Sigma_\nu = \frac{2k_B}{\lambda^2} T_{RJ,\nu} \tag{1}$$

where Σ_ν and $T_{RJ,\nu}$ are functions of both frequency and position. λ is the wavelength corresponding to frequency ν, and $k_B = 1.38 \times 10^{-23}\,\mathrm{J\,K^{-1}}$ is the Boltzmann constant. Eq. (1) can be seen to be based on the Rayleigh-Jeans approximation for black-body radiation (hence the use of the RJ suffix). The specific intensity, I_ν, the energy per unit time per unit frequency per unit area of the detector per unit solid angle, of black-body radiation is given by the Planck law

$$(2) \qquad\qquad I_\nu = \frac{2h\nu^3}{c^2}\left(\exp\left(\frac{h\nu}{k_B T}\right) - 1\right)^{-1}$$

so that at low frequencies ($h\nu \ll k_B T$) $T_{RJ,\nu} = T$, the thermodynamic (radiation) temperature. Nevertheless, the definition of eq. (1) for brightness temperature is used even at high frequencies, where $T_{RJ,\nu} < T$.

It is important to bear in mind this use of brightness temperature because observations of primordial fluctuations in the microwave background radiation (MBR) normally quote results in terms of fractional changes in the thermodynamic temperature $\Delta T/T$, rather than $\Delta T_{RJ,\nu}/T_{RJ,\nu}$, or even $\Delta T_{RJ,\nu}/T$. The relationships between these quantities are complicated for the thermal SZ effect.

It will also be necessary to discuss the polarization of the SZ effects. Polarization in radio astronomy is generally described by the $(I_\nu, Q_\nu, U_\nu, V_\nu)$ Stokes parameters. I_ν is the specific intensity already described, and measures the total energy arriving from the source. (Q_ν, U_ν) describe that part of the energy arriving from the source that is linearly polarized, with a positive value for Q_ν corresponding to vertically polarized radiation dominating over the horizontal polarization. (I_ν, Q_ν, U_ν) together can be used to calculate the linearly polarized flux density fraction, Π_ν, and its position angle, Φ_ν,

$$(3a) \qquad\qquad \Pi_\nu = \frac{\left(Q_\nu^2 + U_\nu^2\right)^{1/2}}{I_\nu}$$

$$(3b) \qquad\qquad \Phi_\nu = \frac{1}{2}\tan^{-1}\left(\frac{U_\nu}{Q_\nu}\right) \quad .$$

while the circular polarization Stokes parameter, V_ν, will not be of interest in this article.

It is useful to express the flux density/brightness temperature relationship for the thermal SZ effect in the usual units of radio astronomy, as

$$(4) \qquad (\Delta S_{\mathrm{th},\nu}/\mu\mathrm{Jy}) = 8.16\,(\Delta T_{\mathrm{th},0}/\mathrm{mK})\,(\nu/\mathrm{GHz})^2\,(\theta/\mathrm{arcmin})^2\,f(\nu, T_{\mathrm{gas}})$$

where $f(\nu, T_{\mathrm{gas}})$ is the spectrum of the SZ effect in brightness temperature terms, normalized to its value at zero frequency. In the Kompaneets approximation,

$$(5) \qquad\qquad f(\nu, T_{\mathrm{gas}}) = \frac{x^2 e^x}{(e^x - 1)^2}\left(2 - \frac{1}{2}x\coth\frac{x}{2}\right)$$

where $x = h\nu/k_B T$, and f is independent of the temperature of the gas in the cluster, T_{gas}. A more precise description of the scattering process (Rephaeli 1995), shows that f is a function of both ν and T_{gas}, and that there are deviations of the spectrum from eq. (5) at high temperature. $\Delta T_{\mathrm{th},0}$ is the zero-frequency brightness temperature change between a line of sight through a cluster and an average line of sight that sees only the unscattered MBR, while $\Delta S_{\mathrm{th},\nu}$ is the flux density difference at frequency ν caused by the thermal SZ effect. A rich cluster of galaxies with $k_B T_{\mathrm{gas}} = 5$ keV might have a central thermal SZ effect $\Delta T_{\mathrm{th},0} = -0.5$ mK at zero frequency. A region with angular radius $\theta = 0.5$ arcmin in the central part of the cluster will then appear with a flux density $\Delta S_{\mathrm{th},\nu} = -0.9$ mJy at 30 GHz (where $\Delta T_{\mathrm{th},\nu} = -0.48$ mK), -6.4 mJy at 110 GHz (-0.26 mK), and $+11.0$ mJy at 350 GHz ($+0.04$ mK) after a null in either flux density or brightness temperature terms at about 218 GHz.

The corresponding kinematic SZ effect, $\Delta T_{\mathrm{kin},\nu}$ is smaller than the thermal effect by a factor

$$(6a) \qquad \frac{\Delta T_{\mathrm{kin},0}}{\Delta T_{\mathrm{th},0}} = \frac{1}{2}\frac{v_z}{c}\left(\frac{m_e c^2}{k_B T_{\mathrm{gas}}}\right)$$

$$(6b) \qquad\qquad = 0.085 \left(v_z/1000 \ \mathrm{km\,s^{-1}}\right) \left(k_B T_{\mathrm{gas}}/10 \ \mathrm{keV}\right)^{-1}$$

at low frequency. Thus if the cluster with $k_B T_{\mathrm{gas}} = 5$ keV and $\Delta T_{\mathrm{th},0} = -0.5$ mK is moving away from the observer with a peculiar radial velocity $v_z = 1000$ km s^{-1}, the kinematic effect will produce signals in a region with angular radius 0.5 arcmin of $\Delta S_{\mathrm{kin},\nu} = -0.15$ mJy ($\Delta T_{\mathrm{kin},\nu} = -83$ μK) at 30 GHz, -1.6 mJy (-63 μK) at 110 GHz, and -1.7 mJy (-7 μK) at 350 GHz, with a maximum flux density effect of -2.8 mJy (-28 μK) near the null of the thermal effect, at about 218 GHz.

While the flux densities for the thermal and kinematic effects are not small by comparison with the sensitivities achievable by (for example) the Very Large Array (VLA) or Australia Telescope Compact Array (ATCA) in a few hours of observing, the relatively large angular sizes on which the effects appear cause considerable difficulties in their detection, as will become apparent later.

Polarization SZ effects arise from a number of causes, including multiple inverse-Compton scatterings within clusters and the transverse or radial peculiar motions of clusters. Recent discussions of polarization terms have been given by Challinor, Ford and Lasenby (2000), and values

$$(7) \qquad\qquad\qquad\qquad \Pi_\nu \sim \tau_e$$

where τ_e is the inverse-Compton scattering optical depth (normally less than 10^{-2}) are typical for multiple scatterings in even the richest clusters of galaxies. Even smaller effects are obtained from single scatterings of the quadrupolar anisotropy, or multiple scatterings of the dipole anisotropy, induced by cluster motions. The detection of such small effects is not yet possible, and so their study must await the development of specialized SZ effect telescopes (Sec. **4˙3**). Nevertheless, such polarization signals would be of considerable

interest since they probe the kinematics of clusters, and so provide information not otherwise available about the development of large-scale structure.

As a final element of jargon associated with SZ observing, it is important to distinguish between the brightness temperature, T_{RJ}, associated with the properties of the radiation field, and the antenna temperature, T_A, measured by a radio telescope. T_A and T_{RJ} are related by an efficiency factor which depends on the ability of the telescope to detect incoming radiation and the relative sizes and shapes of the telescope beam and the source on the sky. For our present purposes we will regard the relationship between the absolute brightnesses of structures seen on the sky and the detected radio power to be a matter of absolute calibration embedded in a generic gain factor G.

1˙2. *Single-dish techniques*. – A single-dish telescope provides an adaptable platform on which to mount a receiver system. While other arrangements are possible, receivers and receiver arrays are generally located at either prime or secondary focus, with the choice of focus depending on the physical size of the receiver, the size of the focal plane that is to be occupied by a receiver array, the gain of the telescope, and the amount of scattered radio power that can be tolerated.

It is useful to begin our analysis of single-dish radiometry by considering the simplest case, of a single beam of solid angle $\Delta\Omega$ aligned with the telescope boresight. A receiver behind such a system will record a power, P, which is not only related to the brightness temperature of the sky within the beam, T_{sky}, but also to any other signals that may appear at the receiver. These inevitably include some emission from the atmosphere and a parasitic ground signal, T_{gnd}, so that

$$(8) \qquad\qquad P = G(T_{\mathrm{sky}} + T_{\mathrm{atm}} + T_{\mathrm{gnd}})$$

and no measure of the incoming power, however carefully calibrated, will be a good measure of the temperature of the sky because of the unknown contributions of T_{atm} and T_{gnd} to P.

The sensitivity of this radiometer system is

$$(9) \qquad\qquad \Delta T_{\mathrm{A}} = \frac{T_{\mathrm{sys}}}{\sqrt{2\,\Delta\nu\,t}}$$

where T_{sys} is the system noise temperature, $\Delta\nu$ is the bandwidth of the receiver, and t is the integration time used. For systems operating at ~ 30 GHz, values of $T_{\mathrm{sys}} \sim 30$ K and $\Delta\nu \sim 1$ GHz are readily obtained, so that the antenna temperature noise after about 1 hour of integration should be $\Delta T_{\mathrm{A}} \sim 11$ μK, and the correponding sky noise (for an antenna with efficiency 0.6) would be $\Delta T_{\mathrm{sky}} \sim 19$ μK. While this estimate suggests that sky temperatures can be measured to high accuracy in a relatively short time, it is hopelessly optimistic. The sensitivity does not improve as $t^{-\frac{1}{2}}$ over long timescales in measurements with a single radiometer because of the varying ground and atmosphere contributions, and because the receiver noise cannot be made "white" over such a long period. Furthermore, the interesting astronomical signal cannot be extracted from the

contaminating atmospheric and ground signals. Thus a different observing technique must be used.

The simplest improvement is to move the observing direction between the point of interest (the target, T) and a reference background region (R) every few seconds. Subtracting the resulting powers should provide a measure of the sky temperature difference between the target and reference region since most of the atmospheric and ground signals should be slow functions of time and position. This technique of *position switching* can provide a good measurement of the temperature difference $T_{\mathrm{sky,T}} - T_{\mathrm{sky,R}}$. The angular separation of the target and reference regions must be sufficiently small that the atmosphere and ground signals are similar at the two locations. However, the differencing scheme then means that only sky structures which differ at the target and reference region can be detected. Since half the observing time is spent on either the target or reference region, and then two noisy measurements have to be subtracted, the maximum sensitivity of the system is a factor 2 worse than the estimate in eq. (9).

A difficulty with this type of observation is that it relies on conditions being stable during the interval between observing the target and reference regions. Since large telescopes tend to move slowly, large changes in the contaminating signals are likely under any but the best conditions, and smaller changes are expected under all conditions because of the varying position of the telescope as it tracks the target across the sky. This problem can be alleviated by moving the beam's position using an oscillating mirror, or a nutating subreflector, rather than by moving the entire telescope. Although this can reduce the position-switching time to a second or less, the moving optics almost inevitably induce systematic differences in the parasitic signals entering the receiver, and there is a mechanical limit to the rate of position-switching.

An alternative strategy is therefore to observe with two beams, provided by two separate feeds. The two feeds are placed symmetrically about the boresight of the telescope, so that the beams have the same shape on the sky, and the target region is placed in one beam (the *main* beam, beam A) while the reference region lies in the other beam (beam B). The signals from these two directions are constantly measured and compared by the receiver system, whose internal switching between the beams can occur on millisecond timescales — sufficiently fast to freeze out atmosphere, ground, and receiver fluctuations. The resulting measurement of

$$(10) \qquad\qquad \Delta P_{AB} = P_A - P_B$$

is averaged over the desired integration time. This *beam-switching* method of observing is faster than position-switching, and reduces the dead time when no data are being taken. Beam-switching can be highly effective because of its superior removal of parasitic signals. A problem that remains is that the target and reference region are being observed with different feeds, and so different systematic errors on the two sides of the receiver can lead to systematic errors in the measurement.

A further improvement is then to combine beam-switching and position-switching. Now an observing cycle of duration t_{cy} is broken into three segments

1. beam A is off target, and beam B is pointed at the target with the difference signal ΔP_{AB} integrated over time $\frac{1}{4}t_{\text{int}}$ ($s_1 = \int \Delta P_{AB}\, dt$);

2. beam A is pointed at the target, and beam B is off target with the difference signal integrated over $\frac{1}{2}t_{\text{int}}$ (s_2); and

3. beam A is off target, and beam B is pointed at the target with the difference signal integrated over $\frac{1}{4}t_{\text{int}}$ (s_3)

and then the best estimate of the sky brightness difference between the target and the average brightness of two reference regions offset to either side of the target is proportional to

$$s = 2s_2 - s_1 - s_3 \quad . \tag{11}$$

This symmetrical switching pattern is relatively efficient at reducing the levels of noise induced by time-varying atmosphere and ground signals, and changing receiver characteristics, since it takes out linear drifts in the behaviour of the system. Typically the integration time, t_{int}, is $(80 - 90)\%$ of the time taken for the complete observing cycle, t_{cy}, with the lost time being taken up by moving the telescope.

It is still necessary to design the equipment to reduce non-ideal behaviour to the maximum extent possible. The receiver should be designed to have similar gains on the two sides with the minimum possible signal losses, and maximum symmetry of illumination of the telescope. The switching scheme should place beams A and B through similar columns of atmosphere, so that switching is generally performed in azimuth. The ground signal can be equalized if the terrain near the telescope is flat and unstructured, or carefully screened, and should be reduced further by designing the feeds to under-illuminate the antenna.

Since the observation of an SZ effect may take a number of hours, spread over a number of days, the positions of the reference beams rotate on the sky about the target to populate *reference arcs* which may extend into a full circle for a circumpolar source (Fig. 1).

As with all astronomical measurements, the observation of an SZ effect will be subject to confusion from foreground and background sources. Beam- and position-switched observing has a higher level of confusion than simple single-beam observing since sources may lie near both the target and reference beam positions. Fortunately, switching in azimuth modulates the confusing signal according to the parallactic angle, p. Contaminated data can then be filtered according to the value of p and removed. With sufficient instantaneous sensitivity, binning by parallactic angle can be used to find and remove even variable sources, which tend to be a large fraction of the source population at the high radio frequencies favoured for SZ effect work.

The discussion above has concentrated on two-beam systems, and a simple position-switching strategy, but this concept can be extended to receiver arrays and more complicated switching schemes designed to remove higher-order systematic effects. Additional
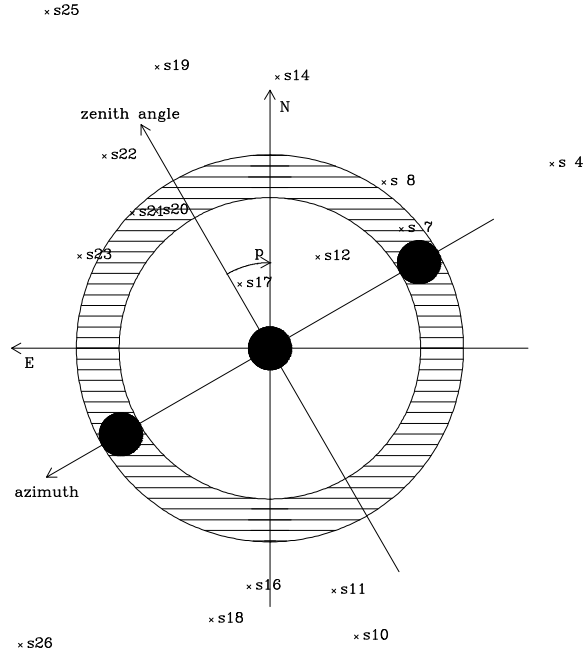
Fig. 1. – Target position, and the development of reference arcs, for OVRO 40-m observations of a point near the centre of Abell 665. The current target and reference positions are shown as solid circles on a line of constant azimuth. As the sky rotates during the observation the reference beams sweep out arcs about the target position. For some parallactic angles, p, these arcs lie near contaminating radio sources: in the configuration shown, the NW reference beam lies near sources s7 and s8.

levels of switching can also be added: for example, identical observations may be made on fields leading and trailing the target field, and the observations can be timed so that the fields are observed over the same range of hour angle. This can remove a residual level of environmental systematic error. The receiver can be rotated, so that the main and reference beams exchange identities, to remove a level of asymmetry in the data caused by imprecise balance in the receiver system. Observations can be conducted at different times of year, so that the position of the Sun and the associated heating of the telescope and ground change, allowing checks for the major spillover signals to be performed.

1˙3. *Single-dish problems*. – Single-dish observations can potentially provide rapid detections of SZ effects, particularly if the telescope is equipped with a radiometer array, but the technique faces three generic problems: of cluster selection, calibration, and confusion.

1˙3.1. Cluster selection. While beam- and position-switching have the advantage of removing the atmosphere and ground signals to good accuracy, they introduce a selection
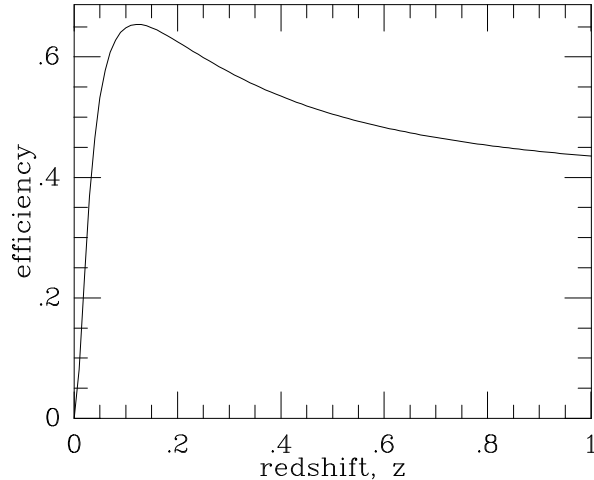
Fig. 2. – The observing efficiency factor, η, as a function of redshift, for observations of clusters with an isothermal β model atmosphere (eq. 25) with core radius 300 kpc and $\beta = 0.67$ by a telescope with a Gaussian beam of 108 arcsec FWHM. The decrease of η is slow at large redshift, and so this observing configuration provides an effective means of detecting clusters at $z > 0.05$ is their intrinsic shape does not evolve.

effect because of the range of angular sizes of SZ effects that can be observed efficiently. SZ effects of small angular size fill only a small fraction of the beam, and so produce only a relatively small signal. SZ effects of large angular size fill not only the target beam, but also the reference beams, so that there is little difference in the brightnesses of the sky in the reference and target beams, so only a small detectable signal. Between these limits there is some angular size, and hence some redshift, for which a given telescope and switching system are most sensitive (Fig. 2).

The selection imposed by this variation of observing efficiency with redshift is relatively simple, and the change of efficiency with redshift is usually slow beyond some redshift of highest sensitivity, so that this is rarely a major problem.

1˙3.2. Calibration. A crucial requirement is that of precise calibration of the brightness scale. Such absolute measurements are essential if the thermal SZ effect is to be used to estimate the value of the Hubble constant, or if the spectrum from a cluster is to be used to separate the thermal and kinematic effects and so to measure the cluster's peculiar radial velocity (Sec. **2**˙5).

Calibration of radio telescopes is usually performed by reference to a set of unresolved radio sources with known flux densities. Absolute measurements of flux densities are possible for only a few extremely bright radio sources, and only sparse flux density measurements have been made. These sources are too bright and too extended to serve as useful calibrators for single-dish (or interferometric) SZ observations. Thus it is necessary to transfer these absolutely-calibrated flux densities to a network of unresolved,

non-variable, secondary calibrators. The interpolation or extrapolation of these known flux densities to the precise frequency of any given SZ effect measurement requires an assumption about the shapes of the sources' spectra. The spectra are generally assumed to be low-order power-laws in $\log S_\nu - \log \nu$ space, but the sparseness of the absolute measurements can make the calibrators' flux densities somewhat uncertain. The combination of this uncertainty and the difficulties of the original absolute calibration are such that the flux density scale in normal use may contain systematic errors at the 5% level.

An alternative is to calibrate the flux density scale using planets, again making some assumption about the types of spectra that they provide, and taking proper account of emission from their atmospheres and surfaces and the variations in brightness across their disks. This is not an entirely straightforward process, and includes issues of polarization effects, the convolution of the brightness distribution of the planet with the shape of the beam, etc., but provides probably the best calibration of the flux density scale for a telescope, with perhaps 3% systematic errors.

If studies of the spectrum of the SZ effect are to be undertaken, then the bandpass in which a given observation is made needs to be well known. In certain frequency ranges the thermal and kinematic SZ effects have relatively steep spectra, and errors in the knowledge of the bandpass can lead to errors in separating the thermal and kinematic components.

It is not enough to make a single calibration of the flux density sensitivity of an antenna, and then to transfer this calibration to an internal noise source that can be used for frequent checks of the system gain. The shapes of large radio telescopes often vary as they move to different parts of the sky, with a corresponding change in their gain, and the measurement of this changing gain is also important if any flux density measurement is to be accurate at the level of a few per cent.

The beamshape of the telescope must also be well known to interpret the results being obtained. This may be a complicated process: for a single dish equipped with a receiver array, the different off-axis angles of the receiver feeds will mean that each beamshape must be independently measured. Each of the beams will also have different polarization characteristics. Both of these properties will change with telescope elevation.

Finally, a continuing, real-time calibration of the data is essential. At cm and mm wavelengths the opacity of the atmosphere changes with time, and a varying optical depth can change the effective sensitivity of the system. To some extent the optical depth can be monitored from the atmospheric brightness (which is reflected in the noise of the measurements), but at the few per cent level it is essential to obtain opacity measurements based on sky dips or independent sky monitoring.

1˙3.3. Confusion. Observations of any structure on the sky are liable to be confused by other foreground or background structures, and the problems of confusion are greater at low angular resolutions and low radio frequencies than at higher resolutions and higher frequencies. Since most SZ effects have arcminute angular scales, the effects of confusion can often be significant and must be taken into account in interpreting the results.

The most basic confusing signal is that of primordial structure in the MBR. Such

signals have a different spectrum from the thermal SZ effects, and so in principle this source of confusion could be removed if sufficiently sensitive data are available at two or more frequencies, and if the relative calibration of the data is good enough. In making this separation, the kinematic SZ effect is also removed since it has the same spectrum as primordial fluctuations in the MBR. MBR confusion is most important at large angular scales, but is likely to be $\sim 10\ \mu$K at the arcminute scales which are of most interest for searches for high-redshift clusters.

Non-thermal radio sources such as quasars and radio galaxies (and star-forming objects, particularly at mm wavelengths) also make an important contribution to the confusion level. The pattern of confusion can be distorted by the gravitational lensing of the cluster, and so can cause a variation in the confusing signal with angle from the cluster centre that mimics the angular structure of the SZ effects. A large fraction of the background radio source population is of steep spectrum, and so these problems can be minimized by observing at short cm wavelengths, or long mm wavelengths. However, a significant fraction of the radio source population is then variable, causing the confusion to change with time and adding further systematic error.

Another possible approach to the reduction of confusion is to detect the confusing sources using a high-resolution interferometer map, and then to remove their flux densities from the SZ effect data collected by the single-dish observations. This approach may run into difficulties by missing resolved radio emission, but such emission usually has a steep spectrum and so is minimized by working at high frequencies. Clusters with strong radio sources are generally so badly contaminated by their emission that no SZ effect measurements are possible. A more significant limitation is the need for frequent interferometric monitoring to deal with variable radio sources, which form a significant fraction of the confusing population at cm wavelengths.

1˙4. *Example single-dish results*. – Early results from single-dish measurements of the thermal SZ effect were subject to many unrecognised sources of error, but the understanding of single-dish data is now good enough that reliable SZ effect detections of high-temperature X-ray clusters can be achieved in a few hours per cluster. As a result, many clusters have been observed by single-dish systems, with random measurement errors $< 100\ \mu$K, and residual systematic errors (for example from radio source confusion) of lower levels.

Some example results (from Birkinshaw 1999) are shown in Fig. 3. It can be seen that good measurements of the amplitudes and angular sizes of the SZ effects of X-ray bright clusters can be made using the beam- and position-switching.

1˙5. *Interferometric techniques*. – The technique of interferometry was originally developed with the intention of achieving high angular resolution, and instruments such as the VLA are examples of this. The SZ effect is primarily a large angular-scale feature on the sky, so high resolution is not of interest and is, in fact, detrimental in this context. However, interferometers offer improvements in the control of systematic effects compared with single-dish telescopes. First, interferometers experience a loss of coher-
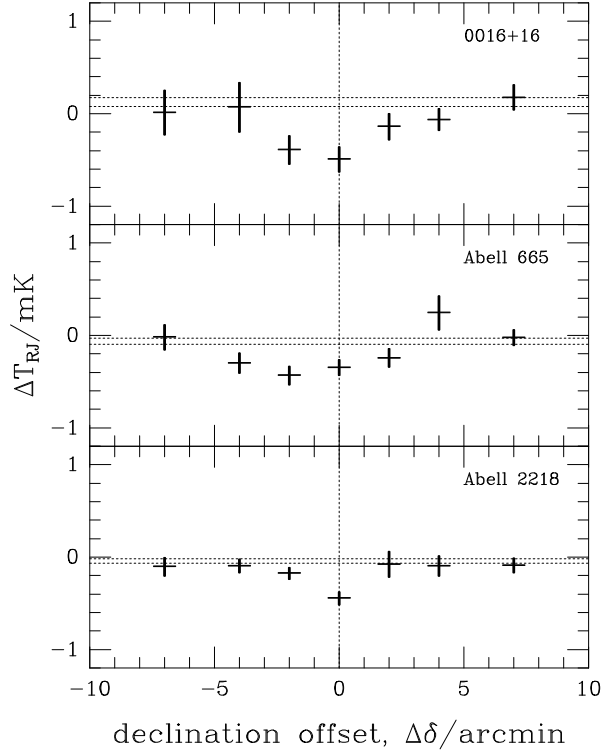
Fig. 3. – Measurements of changes in the apparent brightness temperature of the MBR as a function of declination in the three X-ray bright clusters CL 0016+16, Abell 665, and Abell 2218. The largest SZ effects are seen near the centres of the clusters, and the angular sizes of the effects are consistent with predictions based on the X-ray images. The horizontal lines mark the range of possible systematic errors in the zero levels on the data, and the error bars contain both random and systematic components. The brightness temperature scale is subject to a 5% systematic error.

ence (and thus a loss of sensitivity) away from the pointing centre, meaning that ground spillover, terrestrial interference and other spurious signals will be attenuated. Second, structures on the sky are modulated by a fringe pattern at a different rate than most contaminating sources. This allows rejection of signals from astronomical sources such as the Sun and bright planets. Finally, interferometers with a wide range of baselines allow *simultaneous* observations of confusing, small angular-scale, possibly-variable radio sources, so that their effects can be separated from the SZ signal.

    We can understand the basic principles of interferometry by discussion of a simple case. Consider a two-element interferometer, with antennas separated by a distance b, observing a source at an angle θ, as shown in Fig. 4. Each antenna receives a signal which produces a time-varying voltage, and the product of these voltages is measured. Due to
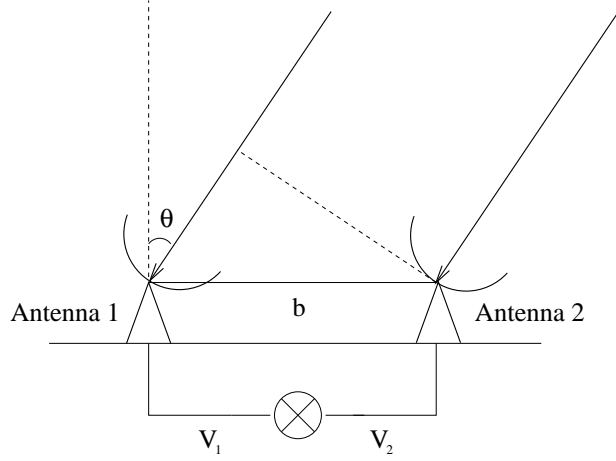
Fig. 4. – A simple one-dimensional interferometer. Radiation from the source must travel an extra distance $b\sin\theta$ to reach antenna 1.

the path difference for radiation travelling from a distant source to the two antennas, there will be a phase difference between the received signals given by

$$(12) \qquad\qquad \phi = 2\pi\frac{b}{\lambda}\sin\theta.$$

The correlated output is then

$$(13a) \qquad\qquad \mathcal{A} = V_1 V_2 \propto \sin(2\pi\nu t)\sin(2\pi\nu t + \phi)$$
$$(13b) \qquad\qquad \propto \cos\phi - \cos(4\pi\nu t) + \sin(4\pi\nu t)\sin\phi \quad.$$

In practice the output $\mathcal{A}$ is integrated over some time interval so that the rapidly-varying second and third terms average to zero. If the energy received from the source per unit area is S, and the area of each antenna is a, the interferometer response is

$$(14) \qquad\qquad \mathcal{A} \propto aS\cos\left(2\pi\frac{b}{\lambda}\sin\theta\right) \quad.$$

Phases are usually not measured absolutely, but relative to some reference direction, θ_0. For a source offset by a small angle $\Delta\theta$ from θ_0, we have $\theta = \theta_0 + \Delta\theta$ and (14) becomes

$$(15a) \qquad\qquad \mathcal{A} \propto aS\cos\left(2\pi\frac{b}{\lambda}\sin(\theta_0 + \Delta\theta) - 2\pi\frac{b}{\lambda}\sin\theta\right)$$
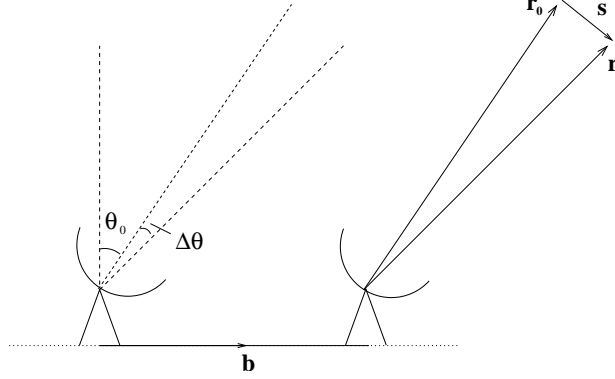$$(15b) \qquad\qquad \propto aS\cos\left(2\pi\frac{b}{\lambda}\Delta\theta\cos\theta_0\right)$$

Fig. 5. – The same simple interferometer as Fig. 4, where the field centre is specified by $\mathbf{r}_0$ and the source position is $\mathbf{r}$. θ_0 and $\Delta\theta$ are the angles discussed in the text.

since we are dealing with small angles. The correlated output differs at different antenna separations, so that the angular resolution of this simple interferometer is proportional to λ/b. A more complex multi-baseline instrument is sensitive to a range of scales determined by the set of baseline lengths defined by the antenna locations. The shortest baseline defines the maximum scale which can be sampled. Sky structures on larger angular scales will not modulate $\mathcal{A}$ with θ_0 (and hence with time), and so will not produce a detected signal.

The interferometer response can be expressed more generally — we consider the main points here, but a full treatment is given in Thompson, Moran and Swenson (1986). If we now specify the source position by a vector $\mathbf{r}$ (see Fig. 5) and the baseline by the vector $\mathbf{b}$, the phase difference from (12) can be written $\phi = (2\pi/\lambda)\mathbf{b}.\mathbf{r}$. The reference direction may be specified by a vector $\mathbf{r}_0$, so that $\mathbf{r} = \mathbf{r}_0 + \mathbf{s}$, where $\mathbf{s}$ describes the shift between the two. After some manipulation, the response to all sources within the solid angle Ω becomes

$$(16) \qquad \mathcal{A} \propto \int e^{-2\pi i \frac{\mathbf{b}.\mathbf{s}}{\lambda}} \, d\Omega \quad .$$

It is conventional to specify the baseline vector $\mathbf{b}$ in terms of right-handed coordinates (u, v, w), where w is in the direction of the source, u and v point East and North respectively as seen from the source position, and distances are measured in wavelengths. Additionally, the position of the source on the sky is usually described in terms of co-ordinates (l, m, n). We see that $\mathbf{b}.\mathbf{r}_0 = w\lambda$, and $\mathbf{b}.\mathbf{r} = (ul + vm + wn)\lambda$, thus $\mathbf{b}.\mathbf{s} = (ul + vm + w(n-1))\,\lambda$. Making the substitution $d\Omega = (dl\,dm)/n$, we find

$$(17) \qquad \mathcal{A} \propto \int dl \int dm\, a(l, m)\, I(l, m)\, \frac{e^{-2\pi i(ul+vm+w(n-1))}}{n}$$

where $a(l, m)$ is the effective total area of the antennas in the direction (l, m) and $I(l, m)$

is the brightness distribution on the sky. $n = (1 - l^2 - m^2)^{1/2} \approx 1$ for small angles, simplifying the Fourier inversion required in eq. (17) to produce a sky map of $I(l, m)$. A map made from interferometer data contains structures which are modulated by the *synthesized beam*. This is given by the Fourier transform of the telescope aperture, which is eq (17) above with the sky brightness replaced by a two-dimensional δ function.

1˙6. *Interferometric problems*. – Despite the many advantages in using interferometric techniques there are numerous complications. Some, like confusion, are of similar type to those affecting single-dish observations, but there are also new problems related to bandwidth, integration time and temperature sensitivity.

1˙6.1. Confusion. Radio source and MBR confusion are difficulties for interferometers just as for single dishes, but interferometric data implicitly contain the possibility of filtering out the confusion from small angular scale radio sources. Short interferometer baselines are sensitive to the SZ effects and to large angular-scale structures in the MBR (Fig. 6) as well as to all nearby radio sources. However features with large angular scale are resolved out on long baselines, and only radio emission from small angular scales produces detectable signal. Thus the confusing radio sources of small angular size can be identified using the longest interferometer baselines, which are insensitive to the SZ effects or MBR structures. The effects of these sources can then be removed on the short baselines by a simple subtraction, allowing SZ effects and other MBR structures to be mapped with much reduced radio source confusion. This is particularly valuable since the *simultaneous* observations of SZ effects and radio sources allows the effects of variable sources to be removed.

This procedure relies on a strong separation between the angular scales of emission from radio sources and the SZ effects, and therefore fails for clusters containing bright extended radio emission (such as radio halo sources). In these cases, the radio emission can be reduced in importance by working at high frequencies (since it is generally of steep spectrum), or by using multi-frequency observations to effect a spectral separation.

1˙6.2. Calibration. Calibration issues for interferometers are effectively the same as those for single dishes, with two caveats. First, interferometers present the additional issue of phase calibration. The electrical length of each baseline will vary slightly from day to day due to instrumental instability (e.g. with ambient temperature), and it is essential to calibrate this in order to retain spatial information in the data. This can be implemented by observation of a bright radio source, and comparison of the fringe rate observed with that calculated from a model situation. Phase corrections can then be applied to the data.

Second, it is simplest to calibrate using radio sources that are unresolved on even the longest baselines, thus reducing the number of suitable calibrators compared to those available for single dish work. MBR interferometers have relatively short baselines, but an additional problem is that their collecting areas are often relatively small, and consequently their flux sensitivity relatively low. For example, the VSA (see Sec. 1˙7) partially resolves the supernova remnants Cas A and Tau A (angular sizes ∼ 5 arcmin, flux densi-
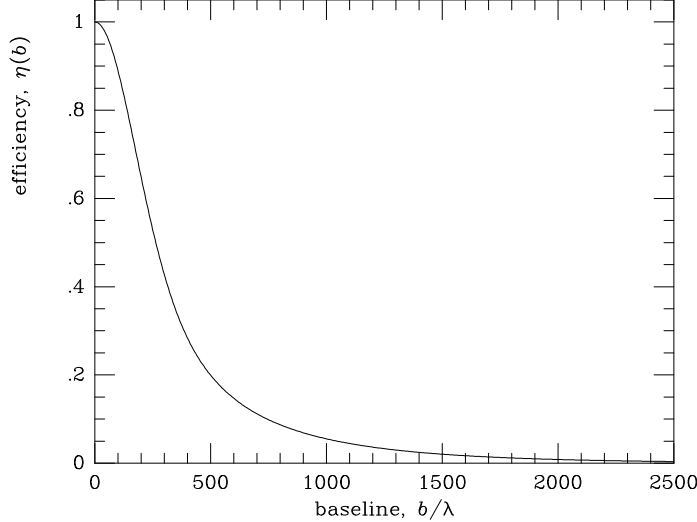
Fig. 6. – Predicted VLA efficiency as a function of baseline for a 5-GHz observation of Abell 665. The shortest baseline available on the VLA is $\approx 800\lambda$, so that most of the SZ effect signal is resolved out by this long-baseline instrument. Since there is no SZ signal on the longest baselines, data on these baselines can be used to obtain accurate flux densities of contaminating radio sources. These flux densities can then be subtracted from the short-baseline data to improve the detectability of the SZ effects.

ties ≈ 180 and 350 mJy at 33 GHz) on its longest baselines, yet the powerful radio galaxy Cyg-A (~ 35 mJy at 33 GHz) is not quite bright enough for accurate phase calibration.

1˙6.3. Bandwidth. In practice an interferometer does not observe at a single frequency ν, but rather over a range $\Delta\nu$ about some central frequency ν_0. This means that the values of (u, v, w), which are measured in wavelengths, change across the passband, reducing the peak signal by a factor

$$
(18) \qquad\qquad \exp\left(-2\left(\pi\frac{\Delta\nu}{\nu_0}\frac{b}{\lambda}\right)^2\right) \quad .
$$

This limits the field size, resolution or bandwidth $\Delta\nu$, which directly affects the sensitivity. To avoid this problem, an interferometer may split the band $\Delta\nu$ into several sub-bands, and deal with each sub-band separately.

1˙6.4. Time constant. Typically, an interferometer will integrate over a few seconds per measurement. This causes off-axis sources to be smeared in arcs in the image plane, again reducing the peak signal. In order to avoid loss of precision, the integration time

$$
(19) \qquad \Delta t \ll \frac{3\ \text{hours}}{\text{number of synthesized beams across field of interest}} \quad .
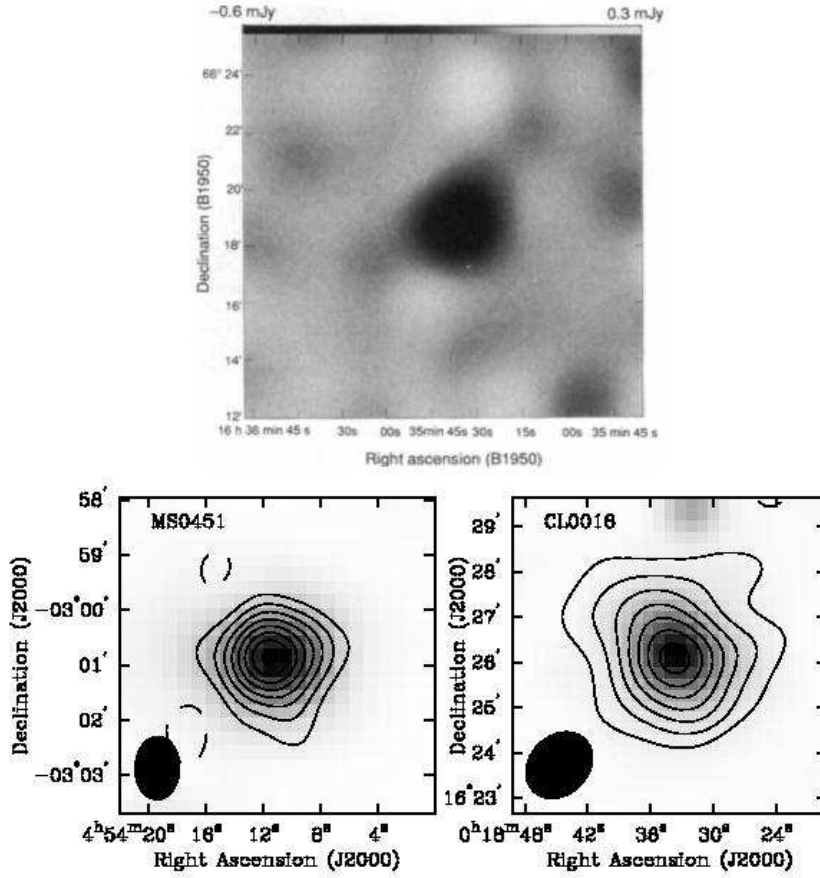$$

Fig. 7. – Top: This Ryle telescope observation of Abell 2218 was the first interferometric detection of the SZ effect. Below: The OVRO and BIMA arrays have also observed many clusters in SZ, including these high significance detections of MS 0451-0354 and CL 0016+16.

This time-constant smearing is only a small effect for CMB interferometers, as their short baselines produce relatively large synthesized beams.

1˙6.5.   Temperature sensitivity. The temperature sensitivity of an interferometer is given by

$$(20) \qquad \Delta T_A \propto \frac{T_{\mathrm{sys}}}{\sqrt{\Delta\nu\, t_{\mathrm{int}}\, N_{\mathrm{corr}}}} \frac{1}{\Omega_{\mathrm{synth}}}$$

(compare eq. 9) where N_{corr} is the number of antenna-antenna correlations used in making the synthesized beam of solid angle Ω_{synth}. This equation shows that sensitivity increases with increased bandwidth and observing time in the same manner as for single-dish

Fig. 8. – The VSA is a dedicated MBR interferometer located at the Observatorio del Teide, Tenerife. Each aperture is about 40 cm in diameter and the table is approximately 3 m across.

observing (t_{int} is made up of many measurements, to eliminate time constant smearing), and also increases with the collecting area of the telescope, as described by the number of antennas. However, for an extended source of angular size θ_s, only antennas separated by baselines less than λ/θ_s contribute to the sensitivity. Longer baselines resolve out the signal, as shown in Fig. 6. The region of high efficiency on this normalized *visibility function* becomes narrower for sources of greater angular extent. As most interferometers are designed for high point source sensitivity, they tend to contain few short baselines. This severely limits sensitivity to the SZ effects, which subtend large (arcmin or greater) angular scales on the sky. One way to reduce this problem is to to observe at longer wavelengths, however confusion from radio sources soon becomes a limiting factor.

Most SZ observations to date have been made using "normal" interferometers, i.e., those designed to achieve high resolution rather than for this purpose. For example, the Berkeley-Illinois-Maryland Array (BIMA), which operates primarily at mm wavelengths, has been used to good effect in its most compact configuration and at cm wavelengths.
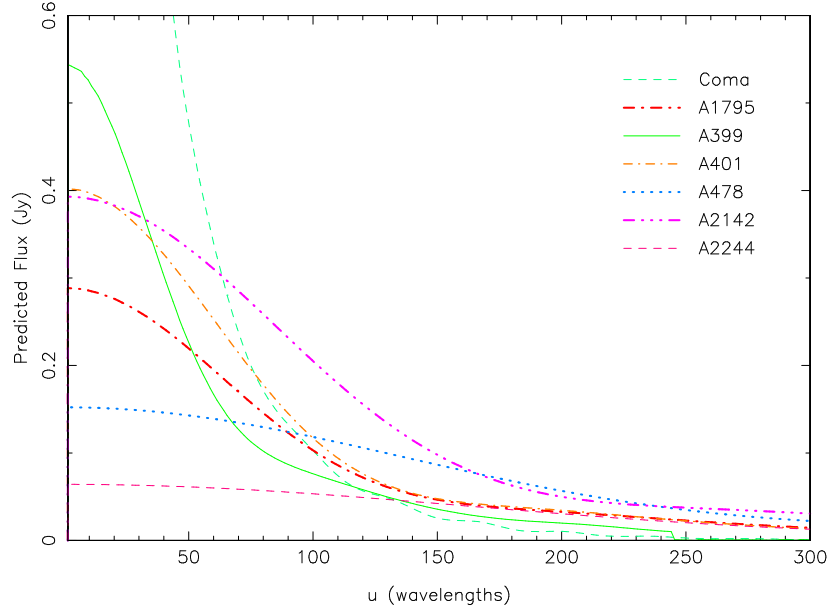
Fig. 9. – Predicted visibilities for VSA measurements of a sample of seven X-ray selected clusters at $z < 0.1$. The shortest VSA baseline is $\approx 40\lambda$.

Since few BIMA baselines were short enough to detect the SZ signal, long integration times were required to achieve appropriate sensitivity.

1˙6.6. Cross-talk. A problem that arises in using compact interferometer configurations is that of antenna-antenna cross-talk, since microwave signals radiated from one antenna can leak into adjacent antennas. Such cross-talk signals can easily dominate the signals expected from SZ effects on the sky. A reduction of this cross-talk is often possible by using the different rates of modulation of the cross-talk and sky signals, at the cost of some loss of data and increased noise.

1˙7. *Example interferometer results*. – The first interferometric map of the SZ effect, shown in Fig. 7, was made by Jones *et al.* (1993) using a Ryle telescope observation of the cluster Abell 2218 which lies at $z \approx 0.17$ (compare Fig. 3). When making a map of such data, it is normal to include only the short baselines where the SZ signal is strongest: longer baselines contribute extra thermal noise, and have already been used to locate and remove a number of confusing radio sources. The result of censoring the baselines is that the maps have limited angular dynamic range. The agreement of the SZ brightness recorded for Abell 2218 with previous single-dish measurements established the credibility of SZ effect research.

The BIMA and Owens Valley Radio Observatory (OVRO) arrays have also made many SZ detections, including CL 0016+16 (BIMA) and a highly significant detection
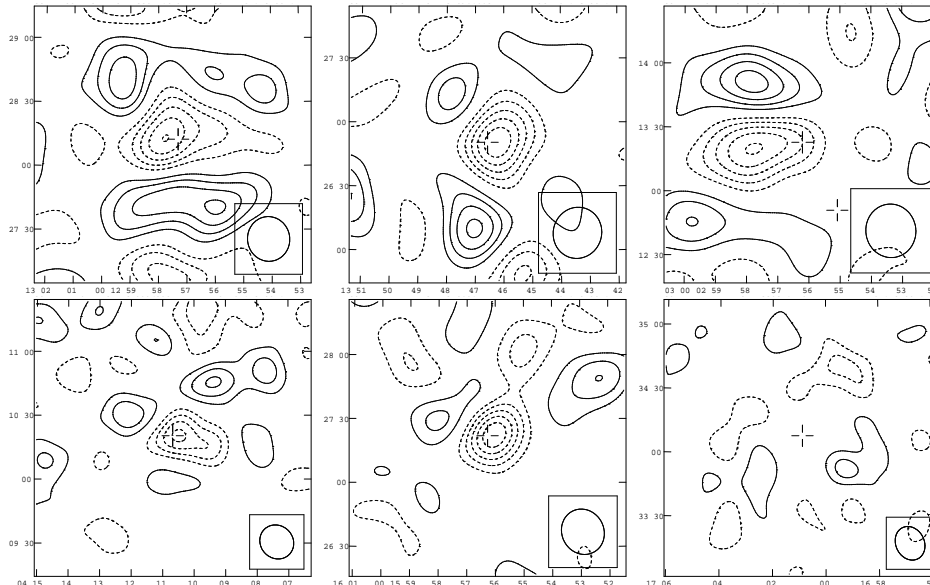
Fig. 10. – VSA maps of seven nearby clusters. Top row, left to right: Coma, Abell 1795, Abell 399/401 (Abell 399 is further south). Bottom row, left to right Abell 478, Abell 2142 and Abell 2244. Coma, Abell 1795, Abell 478 and Abell 2142 are detected. Contamination from the primordial MBR is evident in all maps. Contours are 1.5σ.

of CL 0451-0354 (OVRO). Both are shown in Fig. 7 which was taken from Reese *et al.* (2000). The high signal/noise SZ effect detections apparent in Fig. 7 can be achieved by long and repeated integrations.

The obvious improvement that could improve the quality of SZ observations is to design an interferometer to overcome the difficulties of using "normal" interferometers. Baselines can be tuned for optimum SZ effect detection over some redshift range (i.e. range of angular sizes), and longer baselines can be added to facilitate the removal of radio sources. An example of such a system now in operation is the Very Small Array (VSA; Lancaster *et al.* 2004).

The VSA (Fig. 8), is a table-mounted interferometer run by groups at the Cavendish Laboratory in Cambridge, Jodrell Bank Observatory at the University of Manchester, and the Instituto de Astrofisica de Canarias in Tenerife. The telescope was specifically designed to make observations of both primordial anisotropies in the MBR and SZ effects from galaxy clusters. Its range of baselines ($40\lambda < b < 300\lambda$ at $34\,\text{GHz}$) make it particularly well suited for observing low-redshift clusters, and observations of a sample of low-redshift clusters are presented in Lancaster *et al.* (2004). Fig. 9 shows the predicted VSA visibilities (flux density as a function of baseline; compare Fig. 6) for the seven $z < 0.1$ clusters in this X-ray selected sample.

Each cluster was observed for around 100 hours, resulting in some high signal to

Table I. – *Issues associated with SZ effect studies*

Use	Size of effect (mK)	Critical issues (Sections)
Cluster energetics	0.5	**2**˙1.1
Cluster baryon count	0.5	**2**˙1.1, **2**˙2.1, **2**˙2.2
Cluster gas structure	0.5	**2**˙3.1, **2**˙3.2
Cluster mass distribution	0.5	**2**˙1.1, **2**˙2.1
Cluster radial peculiar velocity	0.05	**2**˙1.1, **2**˙3.2, **2**˙5.1, **2**˙5.2
Cluster Hubble diagram	0.5	**2**˙1.1, **2**˙2.2, **2**˙6.1, **2**˙6.2
Blind surveys and number counts	0.1	**2**˙2.2, **2**˙3.2
Baryon mass fraction evolution	0.1	**2**˙1.1, **2**˙2.1, **2**˙2.2
Microwave background temperature	0.1	**2**˙1.1, **2**˙5.3
Cluster formation studies	0.02	**2**˙1.1
Cluster transverse peculiar velocity	0.01	**2**˙3.2, **2**˙11.1

noise detections, as shown for seven clusters in Fig. 10. All six maps appear noisy — the noise features are confusion from primordial MBR fluctuations, which are relatively powerful on the range of angular scales defined by the baselines used for these maps. Multi–wavelength observations capable of removing the primordial MBR structures are needed for improved sensitivity on these angular scales.

Interferometric SZ observations are now becoming almost routine, even at $z \approx 1$. There have been around 50 cluster detections to date, mostly with non-ideal telescopes, but these are more than adequate to the task. Fig. 11, taken from Carlstrom *et al.* (2002) shows twelve high significance (better than 10σ) examples — many of which have been confirmed by observations with multiple telescopes. The wide range of redshifts of clusters in Fig. 11 demonstrates the potential for using SZ effects to study clusters throughout their histories.

2. – Systematic errors and the science return from Sunyaev-Zel'dovich effect studies

The SZ effects from clusters provide information on the properties of those clusters, and can also be used to obtain important cosmological information. The types of science that can be deduced from SZ effects, and the sizes of the effects that need to be measured, are summarized in Table I. This section summarizes the procedures needed to extract physics from SZ effect measurements, along with the optical and X-ray data that are essential supplements, and how uncertainties in the data impact the science that can be extracted.

2˙1. *Cluster energetics*. – The total thermal SZ effect flux density, $S_{\mathrm{th},\nu}$, from a cluster usually dominates the kinematic effect, so that

$$(21) \qquad S_\nu \approx S_{\mathrm{th},\nu} \propto \int d\Omega \int n_e \, T_{\mathrm{gas}} \, dz \propto U_{\mathrm{th}}$$
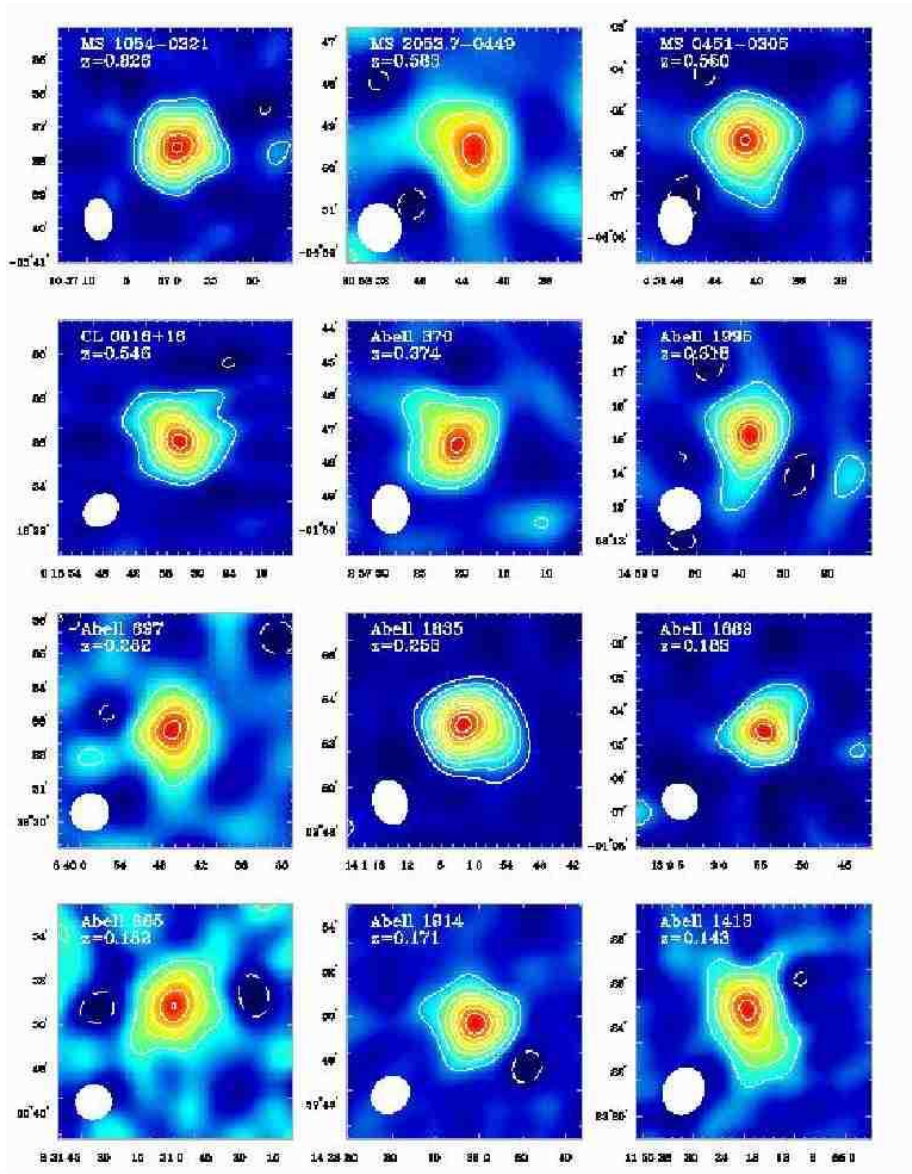
Fig. 11. – OVRO/BIMA maps of galaxy clusters in SZ. Such observations are now becoming routine, often resulting in high–significance detections.

where the integrals are over solid angle and distance along the line of sight, and U_{th} is the total thermal energy content in the atmosphere of the cluster. The constant of proportionality in eq. (21) is composed purely of fundamental constants, the thermodynamic temperature of the MBR, and the frequency of observation, without any cosmological or structural parameters, so that a measurement of the total SZ effect from a cluster immediately provides a model-independent measure of the thermal energy of the cluster gas.

If the gas is in hydrostatic equilibrium in the cluster gravitational potential, then U_{th} should be closely related to the total gravitational potential energy of the cluster, so that an SZ effect survey should be able to pick out clusters of similar masses in similar dynamical states at any redshift. With redshift information from an optical follow-up programme, the evolution of cluster potential wells could be studied and compared with the predictions of cluster formation models.

However, the usefulness of such SZ measurements is critically dependent on the *absolute* calibration of the SZ effect data.

2˙1.1. *Absolute calibrations*. Calibrations of radio data (Secs **1**˙3.2, **1**˙6.2) are often based on measurements of planets, and the conversion from planet measurements at one frequency to the implied flux density from a planet at another frequency depends on the properties of any planetary atmosphere, the surface, and the polarization characteristics of the telescope as well as the precision of the fundamental measurements of planetary flux densities made using absolute instruments.

Generally the complications in planetary observations are relatively minor, so that the residual absolute flux density errors depend on the original absolute calibrations of the planet properties. The radio flux density scale used for SZ effect observations is therefore good to about 5%, and this potential 5% systematic error in the flux density scale should apply to all SZ effect measurements to date.

Space-based observations of SZ effects, for example those to be made by the *Planck* satellite, should be better than this, since they can be calibrated by reference to the MBR dipole anisotropy, which is known from absolute measurements to higher accuracy. A cross-calibration of the planetary scale against the MBR dipole would then allow an improvement to all SZ effect measurements, and reduce their systematic errors significantly.

2˙2. *Cluster baryon count*. – Eq. (21) implies that for a cluster with an isothermal atmosphere

$$(22) \qquad\qquad\qquad S_{\text{th},\nu} \propto N_e T_{\text{gas}}$$

where N_e is the total number of electrons in the cluster. Thus for an isothermal cluster, a model-independent estimate of the total number of electrons in the cluster, and hence the total number of baryons, can be deduced if the temperature, T_{gas}, and metallicity of the cluster gas can be deduced from a good X-ray spectrum.

X-ray data for a cluster can also be used to calculate the cluster's total mass, M_{tot}, using the assumption of hydrostatic equilibrium and spherical symmetry, eq. (23). If this mass estimate is combined with the baryonic mass, taken from N_e deduced from the SZ effect (or from the electron count deduced from the X-ray data), the baryonic mass fraction in the cluster gas, f_{b}, can be found. Since the gas in clusters contains most of the baryons (stars and stellar remnants are a relatively small correction), the value of f_b found in this way should be appropriate for the cluster as a whole (and should be a reliable lower limit). If, then, clusters of galaxies are fair samples of the mass content of the Universe, the derived value of f_b should be close to the value 0.12 ± 0.02 (Turner 2002) for the Universe as a whole.

On the other hand, if clusters are not fair samples of the total matter content of the Universe, then the variation of f_b as a function of redshift, derived by this technique, would be a powerful clue to the processes of cluster formation. At present there is no evidence for significant variations in the cluster-based f_b with redshift (Carlstrom *et al.* 2002), but the errors on the values of f_b are large.

Clearly this measurement can be made only if the calibration of the SZ effect is good (Sec. **2**˙1.1). The measurement also relies on assumptions (Sec. **2**˙2.1) about the gas distribution.

2˙2.1. *Isothermal spherical clusters.* The key assumptions about cluster properties in finding the baryon count are

1. the gas must be isothermal — this is hard to test, since the outer parts of the cluster are X-ray faint, but can make a significant contribution to the SZ effects; and

2. the measurement of the gas temperature must be good — this depends on excellent calibration of the X-ray telescope, and also on the quality of the spectrum since the derived temperature is somewhat dependent on the metallicity of the cluster gas, and this is not usually well determined. For cooler clusters, the nature of the absorbing gas column in our Galaxy will also be important, since the shape of the X-ray spectrum at low energies depends on this column.

The resulting systematic errors in the gas temperature (and it is assumed that the electron and ion temperatures are the same: this is by no means assured) are probably only $(1-2)\%$ in the X-ray bright regions, so the appropriately-weighted systematic error in the gas temperature over the population of electrons and baryons is likely to be only $\sim 4\%$. This is not a major issue.

The strong additional assumption that the cluster has a spherical, or almost spherical, shape is needed if the X-ray data are to be used to determine the total cluster mass and so to determine the cluster baryonic content. Projection effects that could affect the measurement for f_b are a major worry in using this method for individual clusters: a preferable technique would be to apply it for clusters selected in a manner independent of their orientation (i.e., using clusters with surface brightnesses far above some X-ray

threshold, or using clusters from a blind SZ effect survey). The individual measurements of f_b would then be subject to projection effects, but the average f_b can be extracted from the population if the intrinsic distribution of cluster atmosphere shapes can be recovered.

2˙2.2. Large-scale model. The *isothermal β model* of Cavaliere and Fusco-Femiano (1976) is a convenient and frequently-used description of the large-scale structure of the atmosphere of a cluster of galaxies. Its form can be derived from

$$(23) \qquad G\,M_{\mathrm{tot}}(r) = -\frac{k_B T_{\mathrm{gas}} r}{\mu m_{\mathrm{p}}} \left(\frac{d\ln\rho_{\mathrm{gas}}}{d\ln r} + \frac{d\ln T_{\mathrm{gas}}}{d\ln r} \right) \quad .$$

(e.g., Fabricant, Lecar and Gorenstein 1980) which describes how the density, ρ_{gas}, and temperature, T_{gas}, of a gas in hydrostatic equilibrium in a spherically-symmetric gravitational potential well is related to the mass of the cluster, $M_{\mathrm{tot}}(r)$, within radius r. If we assume that the gas is isothermal, and that the total mass distribution has the form

$$(24) \qquad M_{\mathrm{tot}}(r) = 2\,M_{\mathrm{c}} \frac{r^3}{r_{\mathrm{c}}\,(r^2 + r_{\mathrm{c}}^2)}$$

where r_{c}, the core radius, defines a characteristic scale and M_{c} is the mass within r_{c}, then a consistent description of the density of the atmosphere is obtained with

$$(25) \qquad \rho_{\mathrm{gas}} = \rho_0 \left(1 + \frac{r^2}{r_{\mathrm{c}}^2} \right)^{-\frac{3}{2}\beta}$$

where β is a constant which determines the shape of the gas distribution, and depends on the ratio of a characteristic gravitational potential energy and the thermal energy in the gas

$$(26) \qquad \beta = \frac{2}{3} \frac{\mu m_{\mathrm{H}}}{kT} \frac{GM_{\mathrm{c}}}{r_{\mathrm{c}}} \quad .$$

The alternative derivation of this isothermal β model by Cavaliere and Fusco-Femiano (1976) brings out the interpretation of β in terms of the relative scale heights of gas and dark matter in the potential well. Most uses of eq. (25) seek to determine ρ_0, r_{c}, and β without considering the detailed properties of the underlying mass distribution.

It should be noted that the physical consistency of this much-used model for the gas distribution depends on radial symmetry (a simple distortion from a spherical to an elliptical model for the gas density ρ would imply a mass distribution which is not necessarily positive everywhere), and on gas at different heights in the atmosphere having come to the same temperature without having necessarily followed the same thermal history. Eq. (25) is not unique in the sense that gas with a different thermal history might follow a significantly different density distribution. Thus, for example, if the gas

has the same specific entropy at all heights, then the gas density should be described by

$$(27) \qquad \rho_{\text{gas}} = \rho_0 \begin{cases} \left(1 - \alpha \ln \left(1 + \frac{r^2}{r_c^2}\right)\right)^{\frac{1}{\gamma - 1}} & r \leq r_c \left(e^{1/\alpha} - 1\right)^{\frac{1}{2}} \\ 0 & r \geq r_c \left(e^{1/\alpha} - 1\right)^{\frac{1}{2}} \end{cases}$$

where α is a structure constant with a similar meaning to β.

A similar procedure for the mass profile of Navarro, Frenk and White (1995), and an isothermal gas, leads to the gas density distribution

$$(28) \qquad \rho_{\text{gas}} = \rho_{\text{s}} \, 2^{-\alpha} \left(1 + \frac{r}{r_{\text{s}}}\right)^{\alpha \frac{r_{\text{s}}}{r}}$$

where the new structure constant

$$(29) \qquad \alpha = \frac{1}{\ln 2 - \frac{1}{2}} \frac{\mu m_{\text{H}}}{kT} \frac{GM_s}{r_s} \quad .$$

r_s is the scale of the Navarro *et al.* model and M_s is the mass within radius r_s, so that α has a similar physical meaning to β. It can be seen that in this solution $\rho \to \infty$ as $r \to 0$. Examples of eq. (25) and (28) profiles are shown in Fig. 12.

The total masses for both mass distributions in Fig. 12 diverge as $r \to \infty$, so both must be truncated at some outer radius. One possibility is to truncate at r_{200}, the radius at which the mean enclosed mass density is 200× the critical density of the Universe at the redshift at which the cluster is seen.

The run of density and temperature in a cluster atmosphere are usually measured from the X-ray image and spectrum, where a density model for the gas of the form of eq. (25) or eq. (28) is fitted to the X-ray surface brightness. The X-ray surface brightness at a point offset by r in *projected* distance from the centre of the gas distribution (assumed spherical) is (in energy per unit time per unit solid angle per unit frequency)

$$(30) \qquad \Sigma_X(r) = \frac{\int n_{\text{e}} n_{\text{p}} \Lambda(T_{\text{gas}}) dl}{4\pi(1 + z)^3} \quad .$$

where $\Lambda(T_{\text{gas}})$ is the X-ray emissivity of the gas. For an isothermal gas with a β-model density distribution

$$(31) \qquad \Sigma_X(r) = \frac{\Lambda(T_{\text{gas}}) \, n_{\text{e}0} \, n_{\text{p}0} \, r_c}{4 \, \pi \, (1 + z)^3} \left(1 + \frac{r^2}{r_c^2}\right)^{\frac{1}{2} - 3\beta} \sqrt{\pi} \frac{\Gamma(3\beta - \frac{1}{2})}{\Gamma(3\beta)}$$

if the density distribution of eq. (25) is taken to extend to infinity, with a constant gas temperature throughout.

This cannot be a fully physically-consistent description of the atmosphere: it is clearly too simple, as would be the corresponding result for the density distribution of eq. (28).
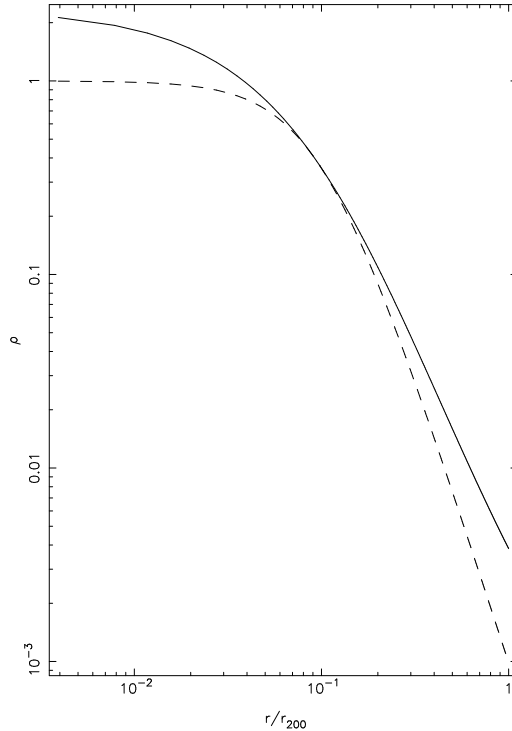
Fig. 12. – Representative isothermal models for cluster atmospheres. Solid line, eq. (28) with $r_s = 0.2r_{200}$ and $\alpha = 10$. Dashed line, eq (25) with $r_c = 0.1r_{200}$ and $\beta = 1$.

Both involve infinite total masses, so an outer cut-off radius (not consistently modelled) is adopted, and eq. (28) also requires an inner cutoff radius. The choice of an isothermal description for the gas is also questionable: what process forces the temperature to become constant, when the gas is accumulated at a number of times from a number of sources (for example, infall and galactic winds), and is imperfectly mixed by galaxy motions or intracluster turbulence?

However, some large-scale gas model like eq. (25) or (28) is essential to relate the X-ray and SZ effects of clusters since X-ray and SZ measurements are sensitive to different parts of the gas distribution. These models also provide a convenient relationship between the atmosphere and the underlying mass distribution. Note that eq. (25) and eq. (28) generally require that the gas constitutes a radially-varying fraction of the total cluster mass.

2˙3. *Cluster gas structure*. – The structures of the atmospheres of clusters of galaxies are generally studied by X-ray rather than SZ techniques at present, since the signal/noise achievable in the X-ray is far superior. However, the X-ray emissivity is proportional to the square of the electron density in the gas rather than to the electron density, so both

the appearance of the X-ray image and the weighting of gas emissivity in the X-ray spectrum are heavily influenced by the centre of the cluster. The SZ effects, on the other hand, are directly proportional to electron density, so they are relatively more sensitive to the outer parts of the clusters and could be better probes of these regions. At present the quality of the SZ data is such that only relatively crude information on the structures of the atmospheres of nearby clusters is available (e.g., Lancaster *et al.* 2004), but the redshift-independence of the SZ effects could make them the best probes of the structures of distant clusters. For the closest clusters, multi-wavelength studies will be needed to remove the "noise" contributed by primordial structure in the MBR.

For simple structural measurements using the thermal SZ effect no absolute calibration is needed, and the X-ray data are useful only if the conversion from the projected electron pressure profile to an electron density profile is of interest. However the extraction of the intrinsic profile from the observed profile relies on a deconvolution with the telescope beam.

2˙3.1.   Beamshape measurements. As discussed in Sec. **1**˙3.1, the telescope beamshape must be well-known for accurate interpretation of the data. There are two types of beamshape measurement that are needed to extract the best science from SZ effect data. First, since clusters generally have a large angular size, they are likely to fill a substantial fraction of the primary beam of an interferometer used to observe the cluster (essentially, this is the same condition as the requirement on the interferometer sampling for the observation to have a high efficiency). This implies that the primary beams of the antennas in the interferometer need to be well known if the SZ effect structure is to be measured well on large angular scales.

On the other hand, small-scale structures are well represented in interferometric data, and for these the beamshape is determined by the sampling of the $u-v$ plane if the phase and amplitude errors in the data are small. Thus small-scale SZ effect structures should be well captured by interferometric observations and the deconvolutions required to find their intrinsic properties should be reliable.

2˙3.2.   Confusion. Structural measurements of this type are clearly subject to confusion. In Sec. **1**˙7 it was shown that primordial structures in the MBR add a degree of noise to an SZ image that cannot be removed without the use of multi-frequency observations to effect a spectral separation of the thermal effect (and this brings in, again, the requirement for high-quality spectral calibration; Sec. **2**˙1.1). This imposes a practical limit on the angular scales of SZ effect structure which can be studied at present.

At smaller angular scales, where the confusion from MBR structures is reduced, confusion from non-thermal radio sources (principally quasars and high-redshift radio galaxies) becomes important (Fig. 1). Removal of most of the effect of these radio sources is feasible using interferometers, as discussed in Sec. **1**˙6.1, by the correct choice of baselines or by aperture-plane fitting. However at the lowest SZ effect flux densities it is hard to remove the confusing sources cleanly.

2˙4. *Cluster mass distribution*. – While it is possible to infer the total mass distribution of a cluster using X-ray data and the assumption of hydrostatic equilibrium (Sec. **2**˙2.2), a better approach may be to use weak lensing. The advantage of this method is that a weak lensing measurement of the ellipticity field induced by a cluster can be converted into a map of the surface mass density of the cluster, Σ_{tot}, which is a linear projection of the total mass density along the line of sight. The ratio of a thermal SZ effect map of the cluster to this Σ_{tot} is then proportional to the projected baryonic mass fraction along each line of sight (if the cluster is isothermal). Simulations (Umetsu *et al.* 2004) show that blank-field SZ effect and lensing maps can provide an estimate of the baryonic content and redshift of clusters detected through either their shear field or their SZ effects.

This use of the SZ effect relies on the absolute calibration (Sec. **2**˙1.1), in order to get the baryonic content, and the assumption of isothermality (Sec. **2**˙2.1), just as the SZ/X-ray approach to the baryon fraction. Otherwise this application is subject principally to the problems of all lensing studies, for example the question of the redshift distribution of the background screen of galaxies and the possibility of multiple structures near the line of sight. While these issues may affect the absolute value of the baryonic content calculated, they should have little effect on the image of the projected baryonic content that can be made, and so the combination of SZ and lensing data may be a useful probe of the large-scale gas-dynamical processes at work in clusters.

2˙5. *Cluster radial peculiar velocity*. – The use of the kinematic SZ effect to measure the radial velocity of a cluster of galaxies relies heavily on the separation of the kinematic and thermal SZ effects. This requires excellent relative spectral calibration (Sec. **2**˙1.1) over a wide range of frequencies — LaRoque *et al.* (2004) fitted the spectrum of Abell 2163 over a decade of frequency in order to obtain their limit on its radial peculiar velocity, and errors in the relative calibration cause errors in the apparent spectral shape of the kinematic effect which can have large effect on the radial velocity.

Since the kinematic effect and primordial structure in the MBR have the same spectrum, the kinematic effect is intrinsically confused by the lumpiness of the MBR (Sec. **2**˙3.2). This confusion limits the velocity accuracy that can be achieved on any single cluster: the level of this limit depends on the angular scale being examined, but exceeds about $200 \ \mathrm{km \, s^{-1}}$ for any plausible present-day observation. Hence the statistical measurement of the radial velocity distribution of clusters of galaxies, as derived from a sample of clusters, is likely to be more useful than the measurement of an apparent radial velocity of any single cluster.

2˙5.1. Bandpass calibration. Since the spectrum of the thermal effect is steeply rising through the null at about 218 GHz, and observations of the intensity of the combined thermal and kinematic effect in this part of the spectrum are usually made using bolometers with wide spectral bandpasses, it is clear that the bandpasses must be well known to avoid distorting the apparent shape of the spectrum. Leakage of power into the detector (principally from higher frequencies) could be a significant source of problems.

2˙5.2.   Cluster velocity substructure. While the kinematic SZ effect is usually discussed in terms of a coherent motion of the entire cluster relative to the Hubble flow, simulations generally show that the largest gas motions arise from substructures within clusters. The largest of these substructures are due to infalling groups, or the residual gas motions from mergers. While this implies that there is significant small-scale kinematic SZ effect structure, which is amenable to interferometric study, the amplitude of individual effects is small, and the superposition of the effects over a large fraction of the cluster tends to produce a level of kinematic effect noise which again reduces the accuracy of any measurement of the overall radial velocity of the cluster. Line-of-sight superpositions of these substructures will also occur, and will tend to confuse their details.

2˙5.3.   Other substructure. We should also note that the assumption of a smooth global mass distribution leading to smooth density and temperature distributions is certainly incorrect. There are a number of substructures found in the X-ray images of clusters which affect the density and temperature locally, and these will change the SZ effects *to the extent that the substructures produce pressure changes*, just as they alter the X-ray appearances of clusters. The (thermal) SZ effect is proportional to the integrated line-of-sight electron pressure, and so a detailed SZ image of a cluster might show

- pressure changes at cold fronts (e.g., as in Abell 2142; Markevitch *et al.* 2000);

- line-of-sight effects from cavities in the gas (e.g., near radio galaxies where radio-faint plasma bubbles are moving, or stationary, in the intracluster medium — note that the non-thermal SZ effect from the relativistic electrons will be too small to compensate for the missing gas even if the bubbles are in pressure equilibrium; Birkinshaw 1999);

- pressure jumps from shocks around infalling groups or sub-clusters, as for example in the case of 1E 0657-56, where temperature and density jumps indicate a substructure moving at Mach 3 through the intracluster medium (Markevitch *et al.* 2002);

- variations in the static models eq. (25, 28) because of the slow changes and temperature gradients associated with cooling flows, which not only involve deviations from hydrostatic equilibrium but which are also likely to be non-steady;

- modest additional SZ effects from the non-thermal scatterings of populations of relativistic particles, particularly those associated with radio halo sources (Liang *et al.* 2002); and

- kinematic SZ effects from motions of substructures in the clusters.

2˙6. *Cluster Hubble diagram*. – One of the major uses to which the thermal SZ effect has been put is that of determining the Hubble constant. In its simplest form, the method

is to compare the X-ray surface brightness and the thermal SZ effect at the centre of a cluster

$$(32a) \qquad\qquad\qquad\qquad \Sigma_{X,0} \propto n_{e,0}^2 \, \Lambda(T_{\text{gas}}) \, r_c$$
$$(32b) \qquad\qquad\qquad\qquad \Delta T_{RJ,0} \propto n_{e,0} \, T_{\text{gas}} \, r_c$$

where r_c is some measure of the scale of the cluster (often the core radius of the best-fitting isothermal β model), and the constants of proportionality include factors from the shapes of the distributions of electron density and electron temperature. The X-ray emissivity of the gas, $\Lambda(T_{\text{gas}})$, is here taken to be a constant over the atmosphere, assuming that the cluster is isothermal and has a constant metal abundance. Then the combination

$$(33) \qquad\qquad\qquad\qquad \Delta T_{RJ,0}^2 \, \Sigma_{X,0}^{-1} \, \Lambda(T_{\text{gas}}) \, T_{\text{gas}}^{-2} \propto r_c$$

and a measure of the angular size of the cluster, θ_c, can be compared with the linear size, r_c, to derive the angular diameter distance of the cluster

$$(34) \qquad\qquad\qquad D_A \propto \Delta T_{RJ,0}^2 \, \Sigma_{X,0}^{-1} \, \Lambda(T_{\text{gas}}) \, T_{\text{gas}}^{-2} \, \theta_c^{-1} \qquad .$$

An example of the application of this method is given in Sec. **3**, but it is clear from eq. (33) that errors in the SZ effect and X-ray temperature have a major impact on the accuracy of the angular diameter distance that is derived. Although the angular diameter distances derived in this way can be used to construct a "cluster Hubble diagram" of angular diameter distance as a function of redshift (Birkinshaw 1999; Carlstrom *et al.* 2002), and in principle this diagram could be used to deduce further cosmological parameters than the Hubble constant, the errors on the distance estimates are currently too large to make this possible.

Clearly a major requirement for the use of this method is that the thermal SZ effect and the X-ray brightness of the cluster are accurately determined: the dominant error is from the SZ effect, since a 5% systematic error in the flux density scale of the SZ effect (Sec. **2˙**1.1) leads to a 10% error in the distance scale. However, if the Hubble constant itself is not of interest, but rather the intention is to use the Hubble diagram to estimate the density parameters $(\Omega_{m0}, \Omega_{\Lambda 0})$, then the absolute calibration not important — it represents merely a shift of the overall distance scale — and only the shape of the angular diameter distance/redshift relation is important.

The large-scale model of the cluster gas (Sec. **2˙**2.2) determines the constant of proportionality in eq. (34), and so it is essential that a correct model is adopted. Since the X-ray data are sensitive to emission from the inner part of the cluster, while the SZ data are relatively more sensitive in the outer regions (because of the different n_e scalings), a high-sensitivity X-ray image of the cluster is essential to trace the gas out to sufficient distance that the model can be used with confidence.

2˙6.1. Clumping. On the smallest angular scales, below the angular resolution of the X-ray image, the gas may be significantly clumped because of the effects of turbulence induced by galaxies moving at transonic speeds, the dissipation of gas from infalling groups, local heating from low-power radio sources, etc. Such clumping has a significant effect on the constant of proportionality in eq. (34). For example, if the clumping is isothermal, then the clumping factor

$$(35) \qquad\qquad C = \frac{\langle n_e^2 \rangle}{\langle n_e \rangle^2}$$

measures the excess of X-ray emissivity over that obtained from a smooth density distribution, and the distance inferred by assuming that the density distribution is smoothed and unclumped is an underestimate by a factor C. Limits to the amount of non-isothermal clumping can be deduced from the detailed X-ray spectrum of a cluster, if the spectrum contains enough counts, but limits on the amount of isothermal clumping can only be based on theoretical considerations about the dissipation time of the implied overpressure and the rate of creation of the clumps.

This issue may induce not only a scale error in the Hubble diagram, and hence an error in the Hubble constant, but could also change the shape of the diagram if the average dynamical state of the intracluster medium evolves with time — perhaps from a clumpy initial state, just after the atmosphere assembles, into a smoother and more relaxed state at the present time. Thus the uncritical use of the cluster Hubble diagram may lead to significant errors in the estimation of the cosmological parameters $(\Omega_{m0}, \Omega_{\Lambda 0})$ that dictate how the angular diameter distance changes with redshift.

2˙6.2. Axial ratio. Eq. (34) derives the angular diameter distance for a cluster by comparing its line-of-sight scale with its transverse angular size. If the cluster is non-spherical, then this ratio will not yield the angular diameter distance correctly. However, if a sample of clusters at similar redshifts, with random orientations, is used, then an average over this sample with its various cluster shapes should reduce the error, at the expense of adding substantially to the noise in the distance estimate.

Such an average will not be successful if the set of clusters is biased, and a bias is likely for the faintest clusters since non-spherical atmospheres have higher central surface brightnesses, and so are easier to detect, if their long axes lie close to the line of sight. It is, therefore, important to select a sample of clusters that has no orientation bias. This can be done either by selecting clusters which are far above the surface brightness limit of some finding survey, or by selecting clusters based on an integrated, surface-brightness independent, indicator of cluster properties. An ideal selection would be the integrated thermal SZ effect, since this is a linear indicator of the total electron count in a cluster, and so is orientation independent.

2˙7. *Blind surveys and number counts*. – SZ-effect selected samples of clusters of galaxies would be ideal for many cosmological purposes, not only for the measurement of the distance scale. This is because the SZ effects are redshift independent in surface

brightness terms, so that clusters can be detected to high redshift. An SZ effect survey could therefore be constructed to be almost mass limited (as shown by the flat efficiency curve in Fig. 2), as well as being orientation independent.

A sample of clusters found by such a survey should therefore provide a fairly direct indicator of how many clusters of a given mass have assembled at any redshift, and the cluster count and redshift distribution can be used to set strong constraints on σ_8 and Ω_{m0} (e.g., Fan and Chiueh 2001) provided that our understanding of the early phases of cluster formation is accurate. Alternatively, we could regard the cluster statistics as a test of our models of cluster formation.

Large surveys for clusters in their SZ effects are only now beginning to be made: up until the present, the sensitivity of interferometers, radiometer arrays, and bolometer arrays has been insufficient to allow surveys of a sufficiently large area of sky for useful statistics on the cluster population to be developed. Perhaps the fastest approaches involve the use of radiometer and bolometer arrays, and the best areas to survey are those which already have significant optical and X-ray coverage (since confirmation of potential cluster detections is a crucial aspect of the work).

Clearly, the absolute calibration of the SZ effects is not a critical issue if the aim of blind surveys is merely to detect clusters, but the surveys will have to contend with the problems of radio source and MBR confusion (Sec. **2**˙3.2). Interpreting the results of the survey must rely on a good knowledge of the selection function: the efficiency of cluster detection as a function of redshift in the presence of MBR fluctuations, radio sources (with a population which evolves with redshift), etc.. The calculation of this selection function will depend on the accuracy of the cluster model (Sec. **2**˙2.2).

2˙8. *Baryon mass fraction evolution*. – This application of SZ effects has been dealt with earlier, for individual clusters (Sec. **2**˙2). The additional difficulty for examining the evolution is only that of knowing the cosmological parameters sufficiently well that the investigation of clusters at different redshifts can work to a constant metric radius, or alternatively to some other well-defined radius (such as r_{200}).

2˙9. *Microwave background temperature*. – The ratio of the thermal SZ effect of a cluster at two different frequencies is a function of the temperature of the MBR, with some slight dependence on the temperature of gas in the cluster and the cluster radial velocity. Thus a precise measurement of the SZ effect spectrum can be used to measure the MBR temperature at distant locations, and over a wide range of redshifts. This would allow a test of the MBR temperature evolution

$$(36) \qquad\qquad\qquad T_{\mathrm{rad}}(z) = T_{\mathrm{rad}}(0)\,(1+z)$$

expected from our normal model of radiation in the Universe. Battistelli *et al.* (2002) found no deviation from eq. (36), but the errors on the SZ effect amplitudes they used were substantial, as were the errors on the MBR temperatures at high redshift (which were obtained from molecular excitation studies). At present this method is relatively insensitive to deviations from eq. (36).

Clearly this technique relies on accurate knowledge of the spectrum of the thermal SZ effect, and therefore on the absence of any significant kinematic SZ effect. Filtering of the effects requires precise knowledge of the relative calibration of the SZ effect data at widely separated frequencies (Sec. **2**˙1.1), and the absence of temperature substructures in the cluster (Sec. **2**˙5.3) large enough to cause significant spectral changes.

2˙10. *Cluster formation studies*. – The SZ effects related to the formation of clusters should be those of lowest brightness and smallest angular size, since they are generated as cluster potential wells begin to accumulate gas, and that gas is heated by the impacts of infalling groups. The angular scales that are relevant are of order 10 arcsec, and the amplitudes of the effects are ~ 20 μK. Such structures are only detectable against the background of MBR confusion because they have a rising power spectrum while primordial MBR fluctuations have a falling spectrum at such small scales (Molnar and Birkinshaw 2000), and because it should be possible to use spectral techniques to separate the thermal SZ effect from primordial fluctuations.

Efforts to look at the first clusters are generally better in the SZ effects than in the X-ray: the SZ effects begin to increase in flux density beyond $z \sim 1.6$ because of the redshift-independence of their surface brightnesses and the behaviour of $D_A(z)$, while it is already difficult to detect high-mass X-ray clusters beyond $z = 1$.

The prospects of detecting the SZ effects of the first clusters are not currently good, since even allowing for the efficiency with which SZ effect surveys can find distant clusters, the amplitude of the thermal signal is low. Indeed, for sufficiently fast infall and sufficiently cool accreting groups, the principal detectable SZ effect may be kinematic rather than thermal, and then the separation from primordial fluctuations in the MBR can only be done statistically (for example using deviations from the expected primordial power spectrum).

Crucial requirements for attempting this work are, therefore, the ability to attempt accurate spectral separation (and hence the requirement for good absolute calibration; Sec. **2**˙1.1), and the development of a suitable telescope for this work (Sec. **4**˙3).

2˙11. *Transverse velocities*. – The transverse velocities of clusters can be extracted from the comparison of the amplitude and polarization of their thermal SZ effects. Even for the brightest SZ cluster, the amplitude of the polarization signal is expected to be under 10 μK, and this polarization (with a uniform direction across the cluster) must be separated from the circumferential pattern of polarization induced by multiple scatterings (Sec. **1**˙1).

Since many of the radio sources contributing to the confusing background are themselves polarized, a first requirement for this observation to be made is that the confusion be well controlled (Sec. **2**˙3.2).

2˙11.1. Polarization calibration. It is clear that excellent polarization calibration of the equipment used will be essential. Attempting to detect sub-μJy polarization signals in the presence of mJy signals from the thermal SZ effect and similar or larger signals from confusing radio sources will require the polarization behaviour of the telescope to
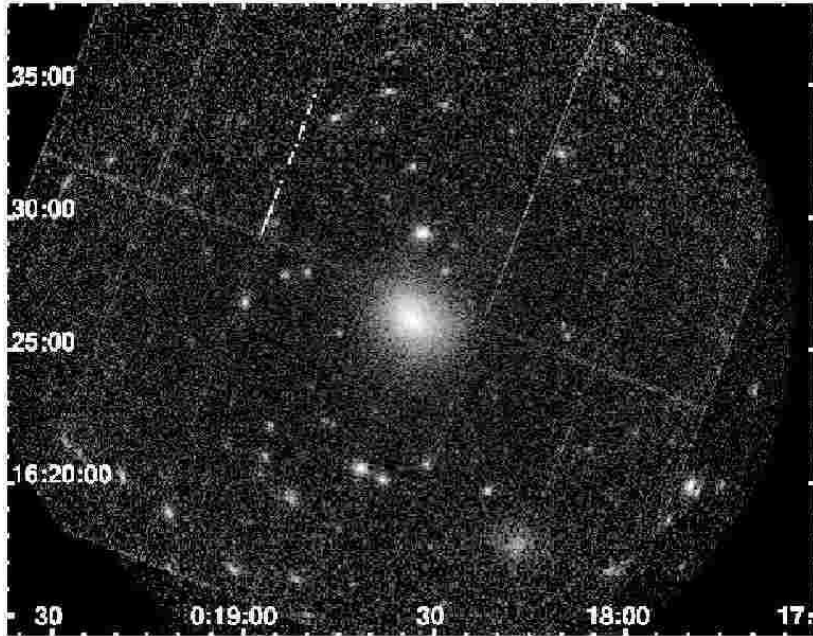
Fig. 13. – Combined MOS-1, MOS-2, and pn image of CL 0016+16 in 0.3 to 5.0 keV, corrected for vignetting but without background subtraction. Artefacts associated with the edges of the chips are evident. CL 0016+16 is the dominant central extended source. The associated quasar and one of the associated companion clusters lie just north and to the south-west, respectively, of CL 0016+16.

be well controlled and the cross-polarization calibrations to be unusually precise. No telescope currently existing is capable of making this measurement on the interesting angular scales: an exploration of the possibilities of polarization measurements may be possible with the next generation of SZ effect telescopes (Sec. **4**˙3).

3. – A case study: CL 0016+16

In this section, we discuss in more detail the procedures that are undertaken to combine SZ effect measurements with other data to extract cosmological and astrophysical information, by reference to the cluster CL 0016+16.

CL 0016+16 was discovered as a candidate high-redshift ($z \sim 0.5$) cluster by Kron (1980). Its basic characteristics in the optical, X-ray, and SZ effect were described by Koo *et al.* (1981), White *et al.* (1981), and Birkinshaw *et al.* (1981) in companion papers. Although the initial discovery was in the optical, this can also be regarded as an X-ray selected cluster, since it appeared independently in the *Einstein* Medium-Sensitivity Survey (Gioia *et al.* 1990).

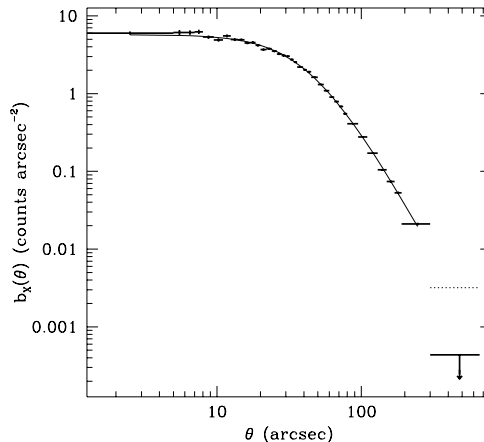Since CL 0016+16 has high optical and X-ray luminosity, and a substantial SZ effect,

Fig. 14. – The 0.3 to 5.0 keV radial profile of CL 0016+16 after subtraction of local background. The curve shows the best-fit circularly symmetric isothermal β model convolved with the point spread function of XMM. The horizontal dotted line shows the range of radii used for local background, and the level of that background.

it has been the subject of a considerable number of studies since the early 1980s. Recent measurements show it to have a redshift of 0.5481 (Ellingson *et al.* 1988), and to be the dominant cluster in a supercluster with at least two adjacent X-ray clusters of lower mass (Hughes *et al.* 1995, Hughes and Birkinshaw 1998). A quasar of similar redshift (Margon *et al.* 1983) also seems to be associated with this supercluster. CL 0016+16 has a $0.5 - 4.5$ keV X-ray luminosity of about 2×10^{38} W.

3'1. *X-ray data.* – *ASCA* and *ROSAT* studies of CL 0016+16 showed the cluster to have a somewhat elliptical shape and a gas temperature of about 7.6 keV (Hughes and Birkinshaw 1998). However the errors on the structural parameters of the gas (β and $\theta_{\rm c}$) in (25) and on the temperature remained a limiting factor in the interpretation of the cluster. *XMM-Newton* observations of the cluster were therefore made to provide better measurements of the properties of the atmosphere. A full description of the treatment of the data is given in Worrall and Birkinshaw (2003).

The *XMM-Newton* observation of CL 0016+16 took 37 ks of data of which rather little was lost to particle flares. An image of the cluster formed from the combined dataset from the three cameras on XMM is shown in Fig. 13. The overall structure of the cluster is somewhat elliptical, but relatively smooth. To first order in the ellipticity we can take the cluster to be circularly-symmetric, and fit the radial profile using the isothermal β model, eq. (25). The fit is good (Fig. 14), and yields structural parameters $\beta = 0.70 \pm 0.01$ and a core radius $\theta_{\rm c} = 36 \pm 1$ arcsec (corresponding to a linear core radius $r_{\rm c} = 240 \pm 10$ kpc in the standard cosmological model).
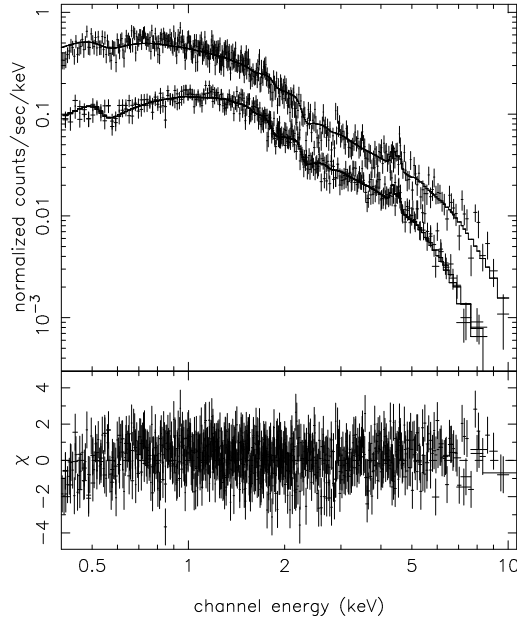
Fig. 15. – The XMM spectrum of CL 0016+16 from a circle of radius 90 arcsec. The upper spectrum is derived from the pn data, while the lower is from the MOS-1 and MOS-2 data. The fit is to an isothermal gas with $k_{\rm B}T = 9.1$ keV, and abundance of 0.22 times the solar value, at the optical redshift of the cluster.

A spectrum of CL 0016+16 extracted from the central part of the cluster is shown in Fig. 15. This spectrum can be well fitted by a single-temperature plasma, with $k_{\rm B}T_{\rm gas} = 9.1 \pm 0.2$ keV and an abundance of 0.22 ± 0.04 times the solar abundance. There are sufficient counts in this spectrum (32600 net counts from the three cameras in $0.3 - 10.0$ keV) that the redshift of the emitting plasma can be determined, and shown to be consistent with the optically-derived redshift of the cluster. It should be noted that there remain uncertainties in the spectral extraction and fitting procedure because of the significant backgrounds in the X-ray images and the complicated distributions of background counts in energy and position on the cameras, and because of residual uncertainties in the calibration.

A further issue is that of structural or thermal substructure in the cluster. A close examination of the central part of the cluster's X-ray image reveals a small central substructure that is also seen in the *Chandra* data. The change in central brightness in the radial profile Fig. 14 due to this central structure is small, so the overall parameters of the β model shouldn't be affected by its presence, but there is some evidence that the central structure is slightly (~ 0.5 keV) hotter than the bulk of the cluster, although the significance is not high.

There are some other variations from the β model profile: in particular there is a region of low surface-brightness emission to the SW of the cluster that is also seen in

TABLE II. – *SZ effect data for CL 0016*

Paper	Telescope	ΔT_{RJ} (mK)
Hughes and Birkinshaw (1998)	OVRO 40-m telescope	-1.20 ± 0.19
Reese *et al.* (2000)	BIMA and OVRO interferometers	-1.24 ± 0.11
Grainge *et al.* (2002)	Ryle telescope	-1.08 ± 0.11
	Converted to XMM model	-1.26 ± 0.07

an earlier ROSAT image (Neumann and Böhringer 1997), but again these brightness structures are too small to affect the overall structural fits.

With the aid of the gas temperature and abundance that are provided by the analysis of the X-ray spectrum, the detected counts can be converted into the central density of the gas in the cluster (conveniently characterised by the central proton density, n_{p0}) if some assumption is made about the cosmology. The derived n_{p0} and $k_B T_{gas}$ are subject to systematic errors from background subtraction uncertainties in both the radial profile and the spectrum, and from our ignorance about small-scale temperature variations in the cluster.

3˙2. *SZ data*. – The SZ effect of CL 0016+16 has been reported many times using a number of different techniques: the large amplitude and angular size of the effect make it a useful test case for new SZ observational programmes. Three recent results are reported in Table II. Of these measurements, one used a large single-dish system equipped with a dual-beam radiometer (Hughes and Birkinshaw 1998), and the other two used interferometers designed for other purposes which had been retro-fitted to provide high sensitivity on large angular scales (Reese *et al.* 2000; Grainge *et al.* 2001).

Although CL 0016+16 has one of the largest SZ effects, in terms of the central surface brightness, the measurements have relatively low signal/noise compared with the X-ray data. β model fits to the SZ data are consistent with the fits obtained from the X-ray data, but add little weight towards improving the errors on the derived structural parameters. Thus it is better to use the X-ray derived structural parameters to fit the SZ data (or to undertake a simultaneous SZ and X-ray fit) than to perform independent fits.

Since the three SZ effects reported in Table II were extracted from the raw data via the application of a different model for the gas, and each model is somewhat different from the model fitted from the X-ray data, it is necessary to correct them to the same overall measure of the SZ effect. The overall result after scalings that take account of the different efficiencies of the observing techniques is that the central SZ effect, at zero frequency, is -1.26 ± 0.07 mK.

3˙3. *Distance of CL 0016+16*. – We can apply the formalism derived in the discussion of the Hubble diagram (Sec. **2**˙6) to estimate the distance of the cluster. The X-ray

emission measure of CL 0016+16, integrated over the entire best-fitting β model, is

$$(37) \qquad \frac{\int n_{e}n_{p}dV}{4\pi D_{L}^{2}} = (1.75 \pm 0.05) \times 10^{21} \quad \text{m}^{-5}$$

and for the isothermal β model we expect that

$$(38) \qquad \frac{\int n_{e}n_{p}dV}{4\pi D_{L}^{2}} = n_{e0}^{2}D_{A} \frac{\theta_{c}^{3}}{\eta(1+z)^{4}} \frac{\sqrt{\pi}}{4} \frac{\Gamma\left(3\beta - \frac{1}{2}\right)}{\Gamma(3\beta)}$$

(as in eq. (31), where η is the electron/proton ratio, taken as being constant over the entire cluster. Since the X-ray data measure β and θ_{c} from the structure of the atmosphere, η (which depends on the abundance of metals in the gas) and T_{gas} from the X-ray spectrum, and the redshift is available either from the X-ray spectrum or optical measurements, the emission measure implies a value for the combination $n_{e0}^{2}D_{A}$ of the unknown central gas density in the cluster and its angular diameter distance.

The central SZ effect of $\Delta T_{RJ,0} = -1.26 \pm 0.07$ mK measures a different combination of gas properties and distance,

$$(39) \qquad \Delta T_{RJ,0} = -n_{e0}D_{A} \, 2\sigma_{T} \, T_{rad} \, \theta c x \frac{k_{B}T_{gas}}{m_{e}c^{2}} \sqrt{\pi} \frac{\Gamma\left(\frac{3}{2}\beta - \frac{1}{2}\right)}{\Gamma\left(\frac{3}{2}\beta\right)}$$

and so $n_{e0}D_{A}$ can be derived from the SZ data. These results can therefore be combined to produce measurements of D_{A} and n_{e0}.

The distance of CL 0016+16 that results is

$$(40) \qquad D_{A} = 1.36 \pm 0.15 \quad \text{Gpc}$$

where the error, at present, is random only. The largest contribution to this random error come from the error on the amplitude of the SZ effect (about 6%, which leads to a 12% error in the distance): an improved measurement of the SZ effect in even this cluster, which has a relatively well-measured SZ effect, would immediately lead to a significant improvement in distance. However, the major issue in absolute distance measurements of this type is not the random error, which could be reduced by continued observations or similar-depth observations of a large number of clusters, but rather the systematic error.

Similarly, a cosmology-independent central electron density can be deduced by combining the X-ray and SZ effect data. The result

$$(41) \qquad n_{e0} = (8.8 \pm 0.5) \times 10^{3} \quad \text{m}^{-3}$$

has a significantly smaller random error than the distance because of the lower power of the SZ effect normalization that appears in the expression for n_{e0}.

Table III. – *Systematic errors in distance measurements*

Class of error	Component	$\sigma_{\mathrm{D}}/D_{\mathrm{A}}$
Calibration	SZ effect amplitude	0.10
	X-ray emission measure	0.05
	X-ray temperature	< 0.02
Projection	3-D shape of cluster	0.20
Substructure	Clumping, shocks, etc.	0.15
Contamination	Kinematic SZ, sources, etc.	0.05
	Quadrature combination	0.25

The systematic errors in the angular diameter distance that arise in the application of this method are summarized in Table III. The major issue for any individual cluster is that of its unknown 3-D shape. Even if we take cluster shapes as being simple oblate or prolate ellipsoids, the possible variations in the estimated distance can be large (e.g., Hughes and Birkinshaw 1998). Additional uncertainty in the X-ray and SZ effect form factors arises because the X-ray measurements are principally sensitive to the central cluster emission (since X-ray emissivity depends on n_{e}^2), while the SZ effect is proportional to n_{e}, and so is relatively more sensitive to the outer regions. Thus changes in shape between the inner and outer parts of the cluster can produce an error in the distance which is effectively unprobed by the X-ray profile even if the structure is spherically-symmetric. For CL 0016+16, where an unusually deep X-ray observation exists, the X-ray data probe to angles < 5 arcmin from the centre, so that about 8 per cent of the central SZ effect originates from larger radii and so is represented in the model used to estimate distance only through an extrapolation of the β model. The fraction of the gas that is unprobed is usually substantially larger than this, leading to a larger potential problem in relating the X-ray and SZ effect data to determine the distance.

Small-scale thermal and density substructure within the cluster can also affect the estimate of distance by boosting the X-ray output relative to the SZ effect (for example by isobaric clumping of the intracluster medium), or by boosting the SZ effect relative to the X-ray output (for example through the existence of regions of shock heating which can cause only small changes in the X-ray spectrum but large local enhancements in electron pressure). The upper limit on the amplitude of these effects in Table III is believed to be conservative, and could be reduced by improved X-ray spectroscopy. However, in a sense this problem could be improved by observing a sample of clusters, since it is unlikely that each will have the same level of substructure. Major outliers could then be detected and removed. For any individual cluster, only simple checks against the presence of substructure in the image (via deviations from Poisson statistics) or in the spectrum (via introducing a distribution of emission measures corresponding to different temperatures) can be made.

Absolute distance measurements like this require absolute calibration of the data used to make the measurements, and so the ultimate reliability of the distances will depend on

the reliability of the calibrations. The largest problem is likely to be in the calibration of the radio flux density scale (as described in Sec. **2**˙1.1), and efforts to improve the calibration of the scale at each of the frequencies used for SZ effect measurement are essential if the distances are to be free from systematic shifts in the distance scale which cannot be identified by sample studies.

If we combine the random and systematic errors on the distance, then the updated result for the angular diameter distance of CL 0016+16 from eq. (40) is

$$(42) \qquad\qquad D_{\mathrm{A}} = (1.36 \pm 0.15) \pm 0.34 \quad \mathrm{Gpc}$$

where the first error is random, and the second systematic. This can be converted into a measurement of the Hubble constant if we make some assumption about the correct cosmology. Adopting a flat cold dark matter cosmology with a cosmological constant contributing 70% of the closure density, we find

$$(43) \qquad\qquad H_0 = (68 \pm 8) \pm 18 \quad \mathrm{km\,s^{-1}\,Mpc^{-1}}$$

which is consistent with the consensus distance scale. The larger value than found in earlier results for CL 0016+16 (which gave a result near $50 \ \mathrm{km\,s^{-1}\,Mpc^{-1}}$) arises almost equally from an increase in the temperature of the gas (from 7.5 to 9.1 keV) and from the change from an open CDM to a flat ΛCDM cosmology.

3˙4. *Lensing and the SZ effect.* – The thermal SZ effect is a linear measure of the line-of-sight thermal energy content of a cluster of galaxies. If the cluster is isothermal and the SZ effect measures the line-of-sight electron density. Thus an SZ effect image can be converted into a map of the line-of-sight integrated baryon density. Since the baryon content of a cluster is dominated by the hot gas in the atmosphere, rather than the baryons in galaxies, an SZ effect image can be converted into a fairly accurate map of the total baryon content of a cluster. This can be compared with the total mass content of the cluster which underlies the gas density model used to fit the SZ effect (or from some deprojected mass model underlying a deprojection of the SZ data) to find baryonic mass fraction of the cluster, and to see whether this changes across the cluster (as it might if there is complicated 3-D structure: potentially this is a way of recovering the 3-D structure of a cluster (Lee and Suto 2004).

More interestingly, the baryonic content map can be compared with the total mass map derived from gravitational lensing to provide a check of the physical description of the mass and gas in the cluster, or to calculate the baryonic mass fraction using the SZ/X-ray derived distance of the cluster rather than the Hubble constant (Sec. **2**˙4).

For CL 0016+16, existing weak lensing data extend only to a radius $\approx \theta_{\mathrm{c}}$ from the cluster centre (Smail *et al.* 1997), so a comparison of the total cluster mass from lensing and implied by the β model is only possible in a cylinder of angular radius θ_{c} (corre-

sponding to a linear scale of about 250 kpc). The mass results are

$$(44) \qquad M_{\text{tot}} = \begin{cases} (2.0 \pm 0.1) \times 10^{14} \text{ M}_\odot & \beta \text{ model, X-ray and SZ data} \\ (2.7 \pm 0.9) \times 10^{14} \text{ M}_\odot & \text{weak lensing} \end{cases}$$

and so are consistent although the lensing mass estimate has a substantial error. By comparison, the total gas mass within the same cylinder is

$$(45) \qquad M_{\text{gas}} = (2.6 \pm 0.2) \times 10^{13} \text{ M}_\odot$$

implying a baryonic mass fraction in the cluster

$$(46) \qquad f_{\text{b}} = 0.13 \pm 0.04$$

which is consistent with the baryonic mass fraction that would be expected from a fair sample of matter in the Universe in the consensus cosmology

$$(47) \qquad \frac{\Omega_{\text{b}}}{\Omega_{\text{m}}} = 0.12 \pm 0.02$$

and shows no sign of evolution compared to nearby high-mass clusters (Carlstrom *et al.* 2002), even though the clusters for which this work has been done do not at present constitute a well-defined sample.

4. – Next steps

The studies of SZ effects to date have largely been performed on relatively poorly-defined samples of clusters selected from ad-hoc lists, often using criteria which could lead to those clusters being unrepresentative of the total population, or even of clusters with identical masses, because of accidental effects of orientation, superposition, or transient dynamical state. Since the SZ effects are linear probes of cluster properties such as total energy content, they should provide excellent, well-defined, samples of clusters and SZ-selected samples would be ideal for such tasks as constructing the cluster-based Hubble diagram or examining the evolution of cluster gravitational potentials.

A major focus of current SZ effect work is therefore to plan for, and conduct, blind surveys of the sky to detect clusters solely through their SZ effects. The full range of observing techniques can be brought to bear on this task, but it is likely that radiometer and bolometer arrays on single dishes will provide the fastest means of performing surveys with arcminute angular resolution over many square degrees of sky.

To date, most SZ effect work has concentrated on simple cluster detection. However, with an increased number of detections, and the prospect of a sample of SZ-selected clusters, it will soon become important to follow up thse detections with higher angular-resolution observations (which are likely to be interferometer-based) to study the state of the gas within and around the selected clusters. Such observations might detect the

kinematic effects from rapidly-infalling filaments, or see substructure from the accretion of filaments or subclusters. Further information can come from polarization observations of clusters showing the brightest SZ effects: measurements of both the radial and transverse velocities of those clusters would provide the dynamical information needed to make detailed tests of cluster formation models.

The requirements of these two programmes are somewhat different, and so distinct types of telescope are needed for surveys and detailed studies. Survey work is probably simplest using bolometer and radiometer arrays (e.g., BOLOCAM or OCRA) although tailored interferometers (e.g., AMI or AMiBA) can also be suitable. Detailed cluster studies will need interferometers or bolometer arrays like SCUBA-2 on large single dishes, since 10 arcsec or better angular resolution is needed. Two examples of specially-designed instruments are OCRA and AMiBA.

4˙1. *OCRA.* – OCRA (Browne *et al.* 2000) was conceived as a 100-element cm-wave radiometer array suitable for mounting at the prime or secondary focus of a large single-dish telescope. A two-beam prototype (OCRA-p) is now operational on the Torun 32-m antenna, with a larger array (OCRA-F) in the final stages of completion. The sensitivity of the full OCRA is such that it could map 100 $\deg^2$ of sky to the confusion limit in a few months, and should generate a sample of clusters of galaxies at all redshifts where they have significant atmospheres, by virtue of the redshift-independence of the brightness temperature change caused by SZ effects.

4˙2. *AMiBA.* – AMiBA (Lo *et al.* 2001), shown in Fig. 16, is a dedicated MBR interferometer designed for rapid surveys of arcminute-scale microwave background structures, including the SZ effects. This ASIAA/NTU project is now replacing the prototype that has been sited on Mauna Loa for the past year with the operational facility.

AMiBA is planned to have 19 antennas of two sizes (diameters 0.3 and 1.2 metres) and will offer a baseline range $380\lambda < b < 1875\lambda$ at 95 GHz. The wide bandwidth at which it operated (~ 20 GHz), and dual-polarization operation, will result in a sensitivity of about 1.3 mJy in one hour, and a range of surveys of different depths is planned to measure the distributions of SZ effects in clusters at a range of redshifts. A simulated AMiBA map, including two SZ detections, is shown in Fig. 17.

4˙3. *The future: the ISZO.* – Survey work requires the coverage of 100 $\deg^2$ or more of sky to a sensitivity of 30 μK or better, and for greatest effectiveness this should be possible in 1 year or less. Bolometer and radiometer arrays, or interferometers, are all potentially capable of making such surveys.

However, it will be important to defeat the confusion limit on such surveys imposed by primordial structure on MBR, and to separate the thermal and kinematic SZ effects. This requires a multi-wavelength survey, and one where the different wavelength bands are well matched in angular resolution and astrometric accuracy. The ideal facility for this type of work would probably be a bolometer array, sited on a single large telescope, with the signals separated by dichroics, and sitting on an excellent site. Experience of
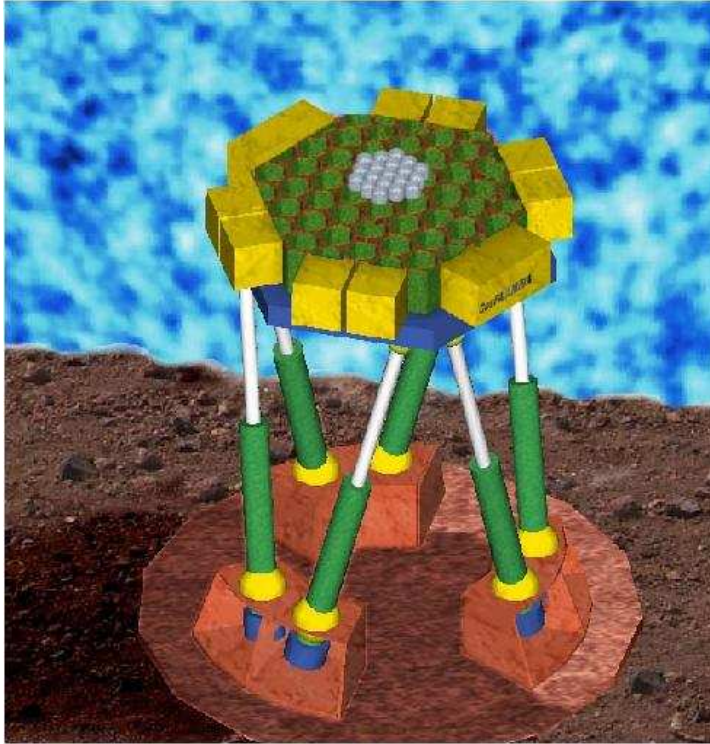
Fig. 16. – Artist's impression of the Array for Microwave Background Anisotropy (AMiBA). The two dish sizes are approximately 0.3 and 1.2 metres in diameter respectively.

such facilities will come from BOLOCAM (Glenn *et al.* 1998) and APEX (Schwan *et al.* 2003).

To study the structures of clusters, it will be necessary to achieve sensitive sub-arcmin scale imaging over fields several arcmin in size. While this is a natural ability of interferometers, it might also be possible to achieve the necessary imaging quality using a bolometer array. Again, multi-wavelength operation will be necessary to separate the different SZ effects and to remove the contamination from radio sources and star-forming galaxies, so that well-matched bolometer arrays or scaled interferometer configurations will be needed. An aim should be access to the velocity channel with a sensitivity $\sim 100 \text{ km s}^{-1}$, which matches the noise imposed by confusion with primordial structures, and some polarization capability, to allow a first investigation of the polarization channel.

Many of these capabilities exist in the current generation of instruments, but it is notable that these instruments are designed at least roughly to match the sensitivity of the current generation of X-ray telescopes. The next generation of X-ray satellites (Con-X and XEUS) will have far higher sensitivity and better spectral capabilities, and so will provide far superior images of clusters of galaxies and of the thermal substructures
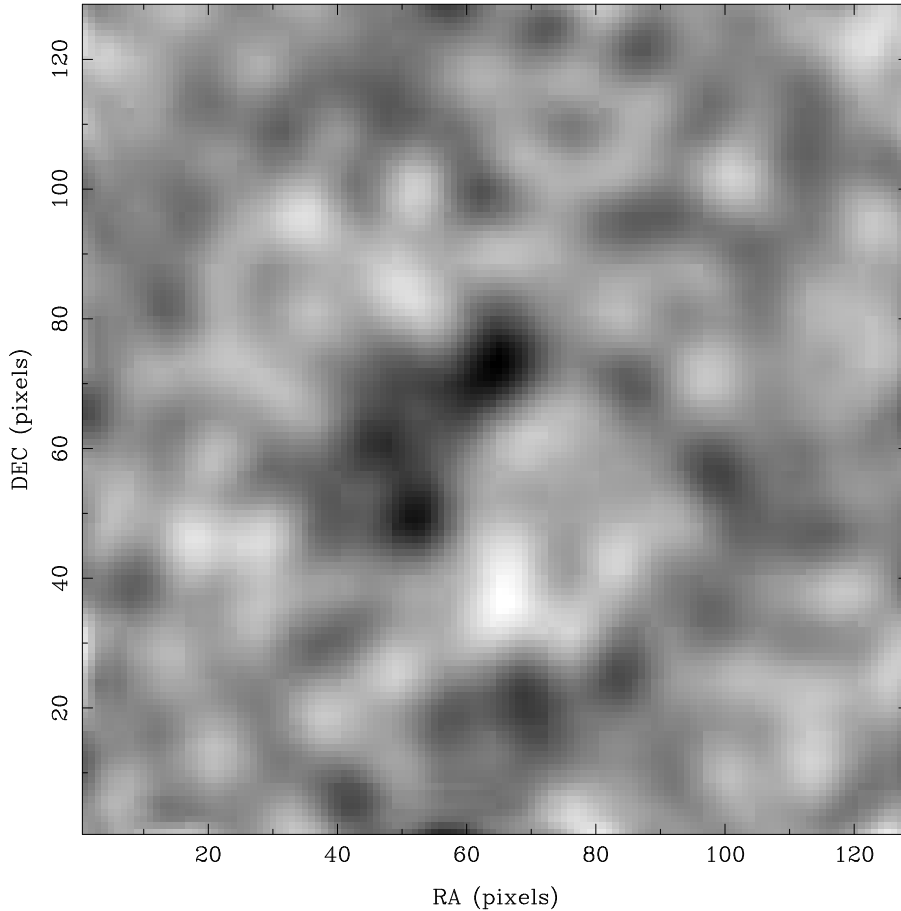
Fig. 17. – A simulated AMiBA field from the planned deep survey, showing two SZ detections.

within them. Now is therefore the time to begin considering an SZ effect telescope that could match these instruments in making detailed studies of cluster substructure and evolution, by achieving at least an order of magnitude improvement in sensitivity over currently-planned systems such as AMI.

One possible design would see the construction of scaled interferometers capable of operation at 30, 90, and 230 GHz (to operate in good atmospheric windows). The scaled design is adopted to permit similar areas of sky to be synthesized at each band: the use of a single telescope design capable of covering all three bands would lead to only small areas of the 230-GHz sky being accessible in a single synthesis. Baselines would be from about $(300 - 10^4)\lambda$, providing ~ 20 arcsec resolution and sensitivity to angular scales as large as 10 arcmin. Individual antennas would be $\sim 300\,\lambda$ in size, to allow close packing at the smallest antenna-antenna separations. About 20% bandwidth at each

band should be possible, but the bands would need to be subdivided to avoid excessive bandwidth smearing. Full polarization capability would allow the polarization channel to be explored (and the sensitivity of the array would allow some other polarization studies of large-scale structures). With ~ 20 antennas and non-uniform antenna separations, good instantaneous sensitivity could be obtained over the full range of angular scales, and with modern receivers the required sensitivity should be achievable.

An alternative design might be to use bolometer arrays at 110, 230, and 345 GHz on a telescope ~ 50 m in size (diffraction limited at the longest wavelength). About 1000 elements would be needed in each array, which is certainly feasible. This design could have high instantaneous sensitivity, making rapid surveys possible.

Either system would be a powerful follow-up to Planck measurements of the SZ effects of some thousands of clusters that we expect, and could provide the deep surveys that would reach to $z > 1$ in the SZ effects. However, both designs involve large-scale projects, and either would require an international team. This concept of an International Sunyaev-Zel'dovich effect Observatory (ISZO) requires considerable work to reach the level of a costed proposal, but it is clear that such an observatory will be a requirement within 10 years to take SZ effect studies to the next level of sophistication and accuracy.

$4^{.}4.$ *Summary.* – Twenty years ago the SZ effects were difficult to measure — although all-sky surveys were achieving excellent sensitivity to the statistical distribution of MBR noise, it was difficult to measure an arcminute-scale structure with a sensitivity of 100 μK, so the existence of the SZ effect from any cluster was questionable.

Ten years ago the thermal SZ effect was regarded as a proven quantity, with possibilities for providing new and interesting cluster and cosmological information.

Today the SZ effects are seen as important windows into cluster formation physics and cosmology, but they are not yet being used fully because it remains difficult to detect any but the most luminous clusters via their thermal SZ effects, and there is insufficient cluster spectral information to make a statistical measure of cluster kinematic SZ effects.

Over the next decade we will enter the era of precise SZ effect measurements, and their routine use in cosmology and astrophysics. It is now important to design the next generation of instruments, for the new era of SZ effect observations, to match the coming generation of high-sensitivity X-ray satellites.

REFERENCES

[1] Battistelli, E.S. *et al.*, *ApJ*, **580** (2002) L101.
[2] Birkinshaw M., *PhysRep*, **310** (1999) 97.
[3] Birkinshaw, M., Gull, S.F., Moffett, A.T., *ApJ*, **251** (1981) L69.
[4] Browne, I.W.A *et al.*, *Proc. SPIE*, **4015** (2000) 299.
[5] Carlstrom, J.E., Holder, G.P., Reese, E.D., *ARAA*, **40** (2002) 643.
[6] Cavaliere A., Fusco-Femiano R., *A&A*, **70** (1978) 677.
[7] Challinor, A.D., Ford, M.T., Lasenby, A.N., *MNRAS*, **312** (2000) 159.

[8] Ellingson, E. *et al.*, *ApJS*, **116** (1988) 247.

[9] Fabricant, D., Lecar, M., Gorenstein, P., *ApJ*, **241** (1980) 552.

[10] Fan, Z. and Chiueh, T,, *ApJ*, **550** (2001) 547.

[11] Gioia I. *et al.*, *ApJS*, **72** (1990) 587.

[12] Glenn, J. *et al.*, *Proc. SPIE*, **3357** (1998) 326.

[13] Grainge, K. *et al.*, *MNRAS*, **239** (2002) 890.

[14] Hughes J.P. and Birkinshaw M., *ApJ*, **501** (1998) 1.

[15] Hughes J.P., Birkinshaw M. and Huchra, J.P., *ApJ*, **448** (1995) L93.

[16] Jones M. *et al.*, *Nature*, **365** (1993) 320.

[17] Koo, D.C., *ApJ*, **251** (1981) L75.

[18] Kron, R.G., PhD thesis, University of California, Berkeley (1980).

[19] Lancaster K. *et al.*, Preprint, `astro-ph/0405582`.

[20] LaRoque, S.J. *et al.*, Preprint (2004).

[21] Lee, J. and Suto, Y., *ApJ*, **601** (2004) 599.

[22] Liang, H., Dogiel, V.A. and Birkinshaw, M., *MNRAS*, **337** (2002) 567.

[23] Lo, K.Y. *et al.*, *IAU Symp.*, **201** (2001) 31.

[24] Markevitch, M. *et al.*, *ApJ*, **541** (2000) 542.

[25] Markevitch, M. *et al.*, *ApJ*, **567** (2002) L27.

[26] Margon, B., Downes, R.A. and Spinrad, H., *Nature*, **301** (1983) 221.

[27] Molnar, S.M. and Birkinshaw, M., *ApJ*, **537** (2000) 542.

[28] Navarro J.F., Frenk C.S. and White S.D.M., *MNRAS*, **275** (1995) 720 and *ApJ*, **490** (1997) 493.

[29] Neumann, D.M. and Böhringer, H., *MNRAS*, **289** (1997) 123.

[30] Reese E.D. *et al.*, *ApJ*, **533** (2000) 38.

[31] Rephaeli, Y., *ARAA*, **33** (1995) 541.

[32] Schwan, D. *et al.*, *NewAR*, **47** (2003) 11.

[33] Smail, I., *et al.*, *ApJ*, **479** (1997) 70.

[34] Thompson A.R., Moran J. M. and Swenson G.W., *Interferometry and Synthesis in Radio Astronomy*, (John Wiley and Sons, Inc.) 1986.

[35] Turner, M.S., *ApJ*, **576** (2002) L101.

[36] Umetsu, I. *et al.*, In preparation.

[37] White, S.D.M., Silk, J.I., Henry, J.P., *ApJ*, **251** (1981) L65.

[38] Worrall D.M. and Birkinshaw M., *MNRAS*, **340** (2003) 1261.